Brillouin Optomechanics

by

Matthew Robert Tomes

A dissertation submitted in partial fulfillment
of the requirements for the degree of
Doctor of Philosophy
(Electrical Engineering)
in The University of Michigan
2013

Doctoral Committee:

Associate Professor Tal E. Carmon, Chair
Associate Professor Xudong Fan
Professor Duncan G. Steel
Professor Herbert G. Winful

ACKNOWLEDGEMENTS

I would like to acknowledge all of the people who have contributed to this work. I would like to thank my girlfriend Kelly Xu for helping me always stay motivated. I would also like to thank my parents, sister, and brother-in-law for their support. My adviser Tal Carmon, worked with and guided my research for the last five years. Other members of my research group provided valuable feedback on my work and helped perform experiments. These members are Hengky Chandrahalim, Kyu Hyun Kim, Mark Dong, and Jeremy Moore. Previous members of our group are Gaurav Bahl, John Zehnpfennig, Tianhe Yang, Xingyu Zhang, and Alex Kaplan. I would like to thank my committee, Professor Steel, Professor Winful, and Professor Fan for their support. I would like to thank my friends in the program: Chris Berry, Paul Stanfield, Yi-Kuei Wu, I-Ning Hu, Cheng Zhu, Momchil Mihnev. Additionally, Michael Schmitt, Oliver Schmitt, and Joel and Katie Schanne.

TABLE OF CONTENTS

LIST OF FIGURES

Figure

CHAPTER I

Introduction

Optical resonators are the basis of any experiment where it is desirable to confine light. The most basic optical resonator, a Fabry-Perot etalon (1), can be as simple as a colorful layer of oil over water, or as complicated as the parallel mirrors in the Laser Interferometer Gravitational-Wave Observatory. When looking for new phenomena, it is often useful to increase intensity. One example is optomechanics (2) which was born after dissipation in resonators was reduced to a level where deformation caused by light pressure became significant (3). Intensity is related to the circulating power over the transverse area of the mode. Whispering gallery resonators can be ideal as they offer quality factors over 100 billion (4) and can confine light to a transverse mode area smaller than a wavelength squared (3). Intensities that would otherwise require pulsed lasers in free space can be achieved in whispering gallery resonators. While previous work in optomechanics relied on the force of light on the device walls, here we use the force of light on an acoustical density wave. Using a silica microsphere, which is a type a whispering gallery resonator (5), we demonstrate a new family of optomechanics based on Brillouin scattering (6). Brillouin scattering is most widely known as a loss mechanism in telecom applications in which stimulated scattering (7) limits the usable power. Here we show that stimulated Brillouin scattering of light from sound can be used as an optomechanical actuation mechanism for high frequency (11 GHz)

acoustical vibrations (8). Owing to ultrahigh optical and mechanical quality factors, we are able to excite mechanical vibrations in Silica whispering gallery resonators at μW input powers and gained for the first time access to mechanical WGM in microresonators. While WGMs were first studied as mechanical phenomena in domed cathedrals, the term is currently used to describe optical modes despite the fact that light does not whisper. Here I enabled access to real (acoustical) whispering gallery modes in microresonators which further enabled us to transform Brillouin scattering into a cooling process. The combination of forward stimulated Brillouin scattering and backward stimulated Brillouin scattering allowed excitation of modes from 50 MHz to 11 GHz in frequency, and enabled for the first time reversing the energy transfer direction in the Brillouin process to allow cooling. I give below a brief overview of the topics covered in each chapter.

1.1 Chapter Overview

Chapter II introduces optical resonators in general and then specifically discusses the whispering gallery resonator.

Chapter III introduces optomechanics and describe previous works in the field.

Chapter IV details the experimental demonstration of lasing via Stimulated Brillouin Scattering in silica WGRs. This chapter has appeared in Physical Review Letters (8). I collaborated with other researches to extend this work and show lasing in the forward scattering configuration (9). I also collaborated on the numerical calculation of the mechanical modes involved (10).

Chapter V continues the study of Brillouin optomechanics by the theoretical calculation of Brillouin cooling. This chapter was published in Physical Review A (11). We performed the experimental realization of Brillouin cooling (12).

Chapter VI gives an additional description of the modes of a whispering gallery resonator. Following B.R. Johnson's analogy of the whispering gallery potential to

atomic potentials (13), we make the first experimental study of tunneling of light from a WGR. This chapter has been published in Optics Express (14).

Chapter VII presents a summary of the additional projects to which I contributed during the course of my degree work. I give a description of forward stimulated Brillouin scattering in microspheres (9). I give an experimental demonstration of cooling via spontaneous Brillouin scattering in microspheres (12). I show the numerical calculation of the mechanical modes involved in stimulated Brillouin scattering in microspheres (10). I introduce a new optomechanical platform based on gyroscopic forces (15). I present an experimental demonstration of fourth harmonic generation and Raman scattering of fourth harmonic generation lines in lithium niobate whispering gallery resonators (16; 17). I introduce an efficient broad band pumping mechanism for on-chip whispering gallery resonators via cascaded energy transfers (18). I theoretically show enhancement of the electric field in a microresonator due to gold nanoparticles being placed in proximity (19).

REFERENCES

[1] H. Kogelnik and T. Li, "Laser beams and resonators," *Proceedings of the IEEE*, vol. 54, no. 10, pp. 1312–1329, 1966.

[2] T. Carmon, H. Rokhsari, L. Yang, T. J. Kippenberg, and K. J. Vahala, "Temporal Behavior of Radiation-Pressure-Induced Vibrations of an Optical Microcavity Phonon Mode," *Phys. Rev. Lett.*, vol. 94, p. 223902, June 2005.

[3] D. Armani, T. Kippenberg, S. Spillane, and K. Vahala, "Ultra-high-Q toroid microcavity on a chip," *Nature*, vol. 421, no. February, pp. 925–928, 2003.

[4] A. a. Savchenkov, A. B. Matsko, V. S. Ilchenko, and L. Maleki, "Optical resonators with ten million finesse.," *Optics express*, vol. 15, pp. 6768–73, May 2007.

[5] D. W. Vernooy, V. S. Ilchenko, H. Mabuchi, E. W. Streed, and H. J. Kimble, "High-Q measurements of fused-silica microspheres in the near infrared," *Optics Letters*, vol. 23, no. 4, pp. 247–249, 1998.

[6] L. Brillouin, "Diffusion of Light and X-rays by a Transparent Homogeneous Body," *Ann. Phys.(Paris)*, vol. 17, p. 88, 1922.

[7] R. Chiao, C. Townes, and B. Stoicheff, "Stimulated Brillouin scattering and coherent generation of intense hypersonic waves," *Physical Review Letters*, vol. 12, no. 21, pp. 592–595, 1964.

[8] M. Tomes and T. Carmon, "Photonic Micro-Electromechanical Systems Vibrating at X-band (11-GHz) Rates," *Physical Review Letters*, vol. 102, p. 113601, Mar. 2009.

[9] G. Bahl, J. Zehnpfennig, M. Tomes, and T. Carmon, "Stimulated optomechanical excitation of surface acoustic waves in a microdevice," *Nature Communications*, vol. 2, p. 403, July 2011.

[10] J. Zehnpfennig, G. Bahl, M. Tomes, and T. Carmon, "Surface optomechanics : calculating optically excited acoustical whispering gallery modes in microspheres," *Optics Express*, vol. 19, no. 15, pp. 14240–14248, 2011.

[11] M. Tomes, F. Marquardt, G. Bahl, and T. Carmon, "Quantum-mechanical theory of optomechanical Brillouin cooling," *Physical Review A*, vol. 84, Dec. 2011.

[12] G. Bahl, M. Tomes, F. Marquardt, and T. Carmon, "Observation of spontaneous Brillouin cooling," *Nature Physics*, vol. 8, pp. 203–207, Jan. 2012.

[13] B. R. Johnson, "Theory of morphology-dependent resonances: shape resonances and width formulas," *Journal of the Optical Society of America A*, vol. 10, p. 343, Feb. 1993.

[14] M. Tomes, K. J. Vahala, and T. Carmon, "Direct imaging of tunneling from a potential well.," *Optics express*, vol. 17, pp. 19160–5, Oct. 2009.

[15] X. Zhang, M. Tomes, and T. Carmon, "Precession optomechanics," *Optics Express*, vol. 19, no. 10, pp. 9066–9073, 2011.

[16] J. Moore, M. Tomes, T. Carmon, and M. Jarrahi, "Continuous-wave ultraviolet emission through fourth-harmonic generation in a whispering- gallery resonator," *Optics Express*, vol. 19, no. 24, pp. 24139–24146, 2011.

[17] J. Moore, M. Tomes, T. Carmon, and M. Jarrahi, "Continuous-wave cascaded-harmonic generation and multi-photon Raman lasing in lithium niobate whispering-gallery resonators," *Applied Physics Letters*, vol. 99, no. 22, p. 221111, 2011.

[18] C. Rotschild, M. Tomes, H. Mendoza, T. Carmon, and M. Baldo, "Cascaded energy transfer for efficient broad-band pumping of high-quality, micro-lasers," *Accepted for publication at Advanced Materials*, 2011.

[19] A. Kaplan, M. Tomes, T. Carmon, M. Kozlov, O. Cohen, G. Bartal, and H. G. L. Schwefel, "Finite element simulation of a perturbed axial-symmetric whispering-gallery mode and its use for intensity enhancement with a nanoparticle coupled to a microtoroid," *Optics Express*, vol. 21, p. 14169, June 2013.

CHAPTER II

Optical Resonators

I will start by discussing optical resonators and their important parameters for Brillouin optomechanics. In breathe mode optomechanics, phase matching is a priori maintained since the created photon (with lower frequency and momentum) is not restricted to a new resonance. Differently, in our Brillouin optomechanics, during the photon generation, the incoming photon loses energy and momentum equal to the created phonon. As resonance enhancement is required for the scattered photon, a resonance is needed that is smaller by $\omega_{phonon}, k_{phonon}$ compared to the optical resonance associated with the incoming light. I will explain the benefits and applications of our resonator configuration which is a circumferentially circulating mode generally referred to as whispering gallery mode. This name follows from an observation by Lord Rayleigh (1).

2.1 Optical Resonators

The most basic optical cavity is a Fabry-Perot etalon named after Charles Fabry and Alfred Perot. In this cavity, two surfaces act as partial mirrors, and there is a fixed separation between them. A soap film is a simple example of a Fabry-Perot etalon as the Fresnel reflections off the two soap surface act as mirrors. The colors we see (Figure 2.1) are evidence of the resonances in the soap layer. More complex

variations can use spherical mirrors to increase the stability and simplify alignment. An example of these two Fabry-Perot resonators are shown in Figure 2.2.

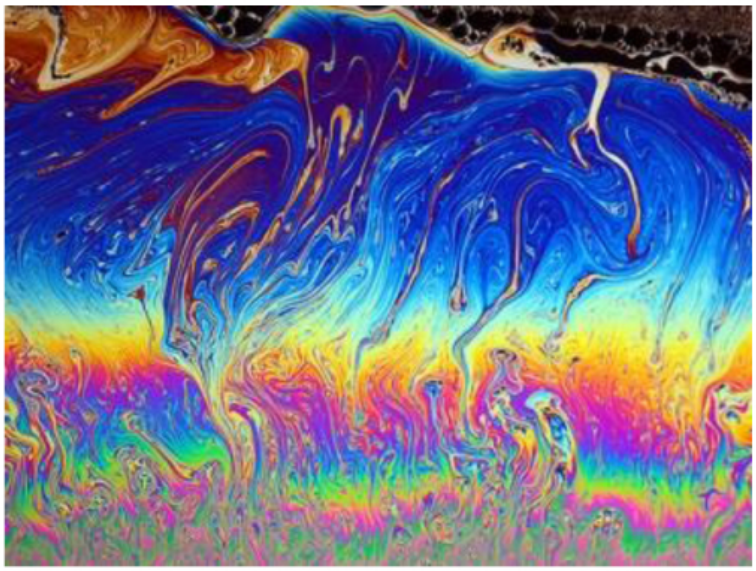

Figure 2.1: Colors seen in a thin layer of soap. Photo credit: Michael Reese Much (http://www.microscopy-uk.org.uk/mag/artmay08/mm-bubbles.html).

Fabry-Perot cavities have resonances when the round trip distance of light in the cavity is an integer number of wavelengths. That means that light traveling through the cavity, reflecting off the first mirror, returning back to the first mirror and reflecting, will be in phase with new light passing through the first mirror. In this manner, the electric field of the incoming light is added constructively (in-phase) with the electric field of the light in the cavity. This leads to a build up of energy in the cavity. This condition can be written in terms of the cavity length, L, and wavelength, λ, where n is an integer.

$$2L = n\lambda. \tag{2.1}$$

For a fixed mirror spacing, there are an large number of wavelengths that satisfy

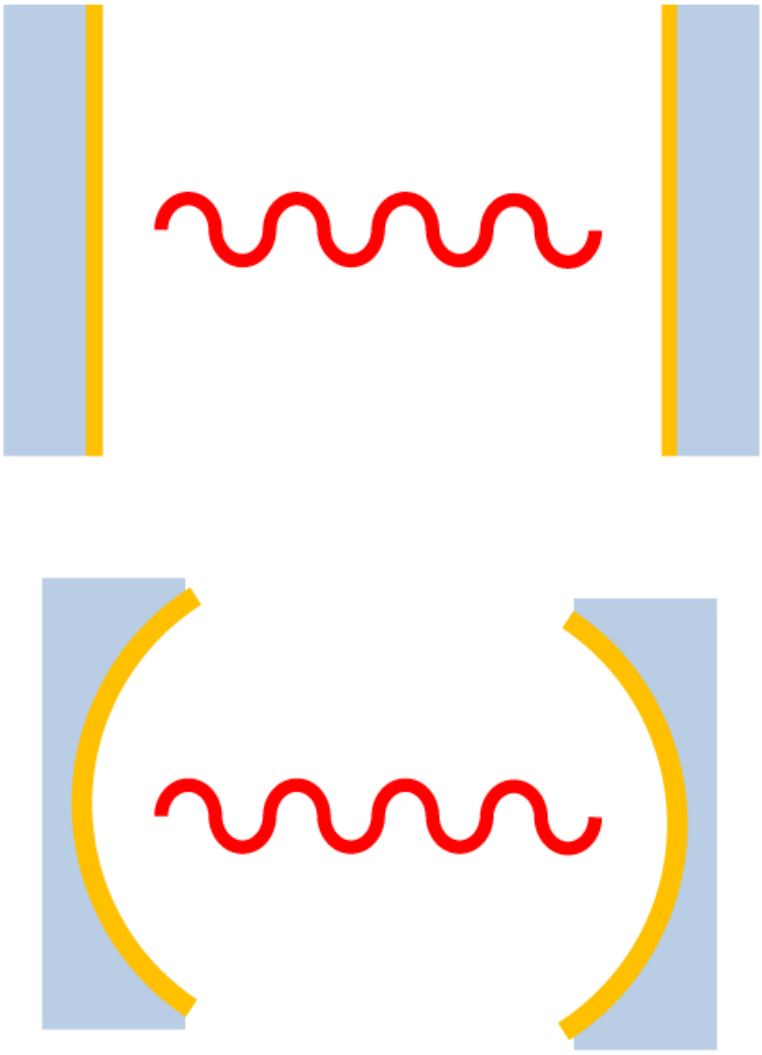

Figure 2.2: Two Faby-Perot cavities using gold coated mirrors. In the upper cavity, light is confined by planar mirrors. In the lower, spherical mirrors are used. The red line represents light in the cavity.

this condition. It is convenient to define the frequency spacing between each successive resonance as the free spectral range (FSR) of the cavity. In a simple two mirror cavity, the FSR is given by,

$$FSR = \frac{c}{2L}, \tag{2.2}$$

where c is the speed of light.

One of the more important functions of an optical cavity is the storage of light. How well a cavity stores light is related to its quality factor Q. The quality factor of a Fabry-Perot resonator is simply the ratio of the energy stored in the resonator to the energy lost per optical cycle.

$$Q = 2\pi \frac{\text{Energy Stored}}{\text{Energy Lost Per Cycle}}. \tag{2.3}$$

In order to have a high quality factor, the amount of loss in the system must be reduced. In Fabry-Perot resonators the quality factor is highly related to the reflectivity of the mirrors used, and the loss of the material between the mirrors. Another related metric is a resonators finesse. In a Fabry-Perot cavity with a lossless medium, the finesse is defined by just the reflectivity, R, of the mirrors.

$$\mathcal{F} = \pi\sqrt{R}/(1-R). \tag{2.4}$$

Quality factor and finesse are dimensionless parameters that describe the loss in a cavity. Quality factor is related to the loss per optical cycle which makes it a loss rate in time. Finesse is related to the loss per round trip which makes it a spacial loss

rate. The quality factor and finesse of a cavity are related by a simple expression,

$$Q = 2\mathcal{F}L/\lambda. \tag{2.5}$$

In most cases, a higher quality factor or finesse is better as it allows more optical power to build up in the cavity. A cavity with a finesse of a million would mean that an incoming photon can circulate 10^6 times before being lost. It also means that a 1 Watt source can be enhanced to 1 megaWatt within the cavity. Obviously, and from energy conservation, we cannot access this 10^6 Watts continuously in time. It is possible to obtain this power for the time associated with 1 round trip in the cavity by essentially breaking the cavity to dump the power. This is referred to as Q-switching. Never the less, photons are indistinguishable particles, and our acoustical density wave can not distinguish if the high intensity originates from a million different photons, a lower number of photons recirculating millions of times through the same cross-sectional area. Thus, for nonlinear optics, having a finesse of 1 million allows us to reduce the threshold for the nonlinear process under investigation by a million. This allows using relatively low power sources to demonstrate nonlinear effects.

In a related manner, the mode volume, V, of an optical cavities is also important. A small mode volume means that the light is confined very tightly. Microcavity and nanocavity are terms for cavities in which the cavity dimensions are on the order of microns and nanometers. Photonic crystal cavities are one type of microcavity. In photonic crystal resonators, light is confined by a photonic band gap where the frequency of interest cannot propagate. This allows for confining light to very small optical mode volumes (2). Another type of microresonator that has small mode volume is the microtoroid (3). The microtoroid is a type of whispering gallery resonator.

2.2 Optical WGRs

In optical whispering gallery resonators, light is allowed to propagate in a circular trajectory. For example, light could propagate around the equator of a sphere. The circumference of the sphere is such that there is an integer number of wavelengths circling it. This allows multiple re-circulations to interfere constructively. They were first discovered by Lord Rayleigh in a domed cathedral. He reported on wave theories for these resonances in 1910 (1). Although Lord Rayleigh's observation was of sound traveling in a circular trajectory, this type of mode can also be observed in the electromagnetic domain (4; 5). For example, an optical wave can be totally internally reflected while traveling around the circumference of a glass sphere.. Optical whispering galleries have been shown to have quality factors as high as 10^{11}, and finesses as large as 10^7 in CaF_2 (6). Another common material for optical whispering galleries is fused silica. Fused silica WGRs are useful as they can be fabricated on-chip in toroidal (3) or spherical (7) geometries, and coupled to with tapered fibers (8; 9; 10). Fused silica has allowed quality factors as high as $8x10^9$ and finesses of $2.2x10^6$ in fiber-tip microspheres (11).

Whispering gallery resonators have been used in a large number of experiments. In 1991, Whispering gallery were shown to lase in 3 to 10 μm micro disks (12). Whispering gallery were also shown to support lasing in neodymium doped silica spheres (13). Nonlinear interactions have been widely studied in whispering galleries due to their high Q and low mode volume. This includes Raman lasing (14), four-wave mixing (15), third harmonic generation (16), fourth harmonic generation (17; 18). Additionally, whispering gallery resonators were shown to demonstration radiation pressure induced mechanical oscillations (19). In this dissertation, I will present another type of mechanical oscillators in whispering gallery resonators, excited by electrostriction. Table 2.1 outlines my contributions to the field of microresonators.

	Opto-mechanics	**Lasers**	**Nonlinear Optics**	**Modal Geometry**
Previous Work	Breathe mode toroids(19)	Raman(20) Erbium(21) Ytterbium(22)	Four-wave mixing(15) Third harmonic generation(16)	Mode calculations (23) Level crossing(24)
My contributions	Mechanical WGM(25)	Brillouin(25)	Fourth harmonic generation(17)	Tunneling(26)

Table 2.1: Continuous wave phenomena in microresonators: Previous state of microtoroid and microsphere research along with my experimental contributions to the fields.

REFERENCES

[1] L. Rayleigh, "The problem of the whispering gallery," *Philos. Mag.*, vol. 20, no. Series 6, pp. 1001–1004, 1910.

[2] Y. Akahane, T. Asano, and B.-s. Song, "High-Q photonic nanocavity in a two-dimensional photonic crystal," *Nature*, vol. 425, no. October, pp. 944–947, 2003.

[3] D. Armani, T. Kippenberg, S. Spillane, and K. Vahala, "Ultra-high-Q toroid microcavity on a chip," *Nature*, vol. 421, no. February, pp. 925–928, 2003.

[4] G. Mie, "Beitrage zur Optik truber Medien, speziell kolloidaler Metallosungen; von Gustav Mie," *Annalen Der Physik*, vol. 25, no. 3, pp. 377–445, 1908.

[5] P. Debye, "Der Lichtdruck auf Kugeln von beliebigem Material," *Annalen Der Physik*, vol. 335, no. 11, pp. 57–136, 1909.

[6] A. a. Savchenkov, A. B. Matsko, V. S. Ilchenko, and L. Maleki, "Optical resonators with ten million finesse.," *Optics express*, vol. 15, pp. 6768–73, May 2007.

[7] T. Carmon and K. J. Vahala, "Modal Spectroscopy of Optoexcited Vibrations of a Micron-Scale On-Chip Resonator at Greater than 1 GHz Frequency," *Physical Review Letters*, vol. 98, p. 123901, Mar. 2007.

[8] J. C. Knight, G. Cheung, F. Jacques, and T. a. Birks, "Phase-matched excitation of whispering-gallery-mode resonances by a fiber taper.," *Optics letters*, vol. 22, pp. 1129–31, Aug. 1997.

[9] M. Cai and K. Vahala, "Highly efficient hybrid fiber taper coupled microsphere laser.," *Optics letters*, vol. 26, pp. 884–6, June 2001.

[10] S. Spillane, T. Kippenberg, O. Painter, and K. Vahala, "Ideality in a Fiber-Taper-Coupled Microresonator System for Application to Cavity Quantum Electrodynamics," *Physical Review Letters*, vol. 91, pp. 2–5, July 2003.

[11] D. W. Vernooy, V. S. Ilchenko, H. Mabuchi, E. W. Streed, and H. J. Kimble, "High-Q measurements of fused-silica microspheres in the near infrared," *Optics Letters*, vol. 23, no. 4, pp. 247–249, 1998.

[12] S. L. McCall, a. F. J. Levi, R. E. Slusher, S. J. Pearton, and R. a. Logan, "Whispering-gallery mode microdisk lasers," *Applied Physics Letters*, vol. 60, no. 3, p. 289, 1992.

[13] V. Sandoghdar, F. Treussart, J. Hare, V. Lefèvre-Seguin, J. Raimond, and S. Haroche, "Very low threshold whispering-gallery-mode microsphere laser.," *Physical review. A*, vol. 54, pp. R1777–R1780, Sept. 1996.

[14] B. Min, T. J. Kippenberg, and K. J. Vahala, "Compact, fiber-compatible, cascaded Raman laser.," *Optics letters*, vol. 28, pp. 1507–9, Sept. 2003.

[15] T. Kippenberg, S. Spillane, and K. Vahala, "Kerr-Nonlinearity Optical Parametric Oscillation in an Ultrahigh-Q Toroid Microcavity," *Physical Review Letters*, vol. 93, pp. 18–21, Aug. 2004.

[16] T. Carmon and K. Vahala, "Visible continuous emission from a silica microphotonic device by third-harmonic generation," *Nature Physics*, vol. 3, no. 6, pp. 430–435, 2007.

[17] J. Moore, M. Tomes, T. Carmon, and M. Jarrahi, "Continuous-wave ultraviolet emission through fourth-harmonic generation in a whispering- gallery resonator," *Optics Express*, vol. 19, no. 24, pp. 24139–24146, 2011.

[18] J. Moore, M. Tomes, T. Carmon, and M. Jarrahi, "Continuous-wave cascaded-harmonic generation and multi-photon Raman lasing in lithium niobate whispering-gallery resonators," *Applied Physics Letters*, vol. 99, no. 22, p. 221111, 2011.

[19] T. Carmon, H. Rokhsari, L. Yang, T. J. Kippenberg, and K. J. Vahala, "Temporal Behavior of Radiation-Pressure-Induced Vibrations of an Optical Microcavity Phonon Mode," *Phys. Rev. Lett.*, vol. 94, p. 223902, June 2005.

[20] L. Yang, T. Carmon, B. Min, S. Spillane, and KJ, "Erbium-doped and Raman microlasers on a silicon chip fabricated by the solgel process," *Applied Physics*, vol. 86, 2005.

[21] T. Kippenberg, J. Kalkman, a. Polman, and K. Vahala, "Demonstration of an erbium-doped microdisk laser on a silicon chip," *Physical Review A*, vol. 74, p. 051802, Nov. 2006.

[22] E. P. Ostby, L. Yang, and K. J. Vahala, "Ultralow-threshold Yb(3+):SiO(2) glass laser fabricated by the solgel process.," *Optics letters*, vol. 32, pp. 2650–2, Sept. 2007.

[23] M. Oxborrow, "Traceable 2-D Finite-Element Simulation of the Whispering-Gallery Modes of Axisymmetric Electromagnetic Resonators," *IEEE Transactions on Microwave Theory and Techniques*, vol. 55, no. 6, pp. 1209–1218, 2006.

[24] T. Carmon, H. G. L. Schwefel, L. Yang, M. Oxborrow, A. D. Stone, and K. J. Vahala, "Static Envelope Patterns in Composite Resonances Generated by Level Crossing in Optical Toroidal Microcavities," *Physical Review Letters*, vol. 100, p. 103905, Mar. 2008.

[25] M. Tomes and T. Carmon, "Photonic Micro-Electromechanical Systems Vibrating at X-band (11-GHz) Rates," *Physical Review Letters*, vol. 102, p. 113601, Mar. 2009.

[26] M. Tomes, K. J. Vahala, and T. Carmon, "Direct imaging of tunneling from a potential well.," *Optics express*, vol. 17, pp. 19160–5, Oct. 2009.

CHAPTER III

Optomechanics

3.1 Background

When light induces and is affected by mechanical motion at a structural level the resulting effects are termed optomechanics. This coupling between light and structure was predicted as early as 1970 by Braginsky (1) as a noise mechanism in gravitational wave detectors. Recent advances in dissipation reduction and miniaturization of optical resonators has led to the first experimental demonstration of vibrations actuated by the pressure of light in 2005 (2).

To understand the principle of optomechanics, it is useful to imagine a simple Fabry-Perot resonator with two mirrors. One of the mirrors is fixed firmly in place while the other mirror is attached to a mechanical spring. When light builds up in this cavity, momentum conservation considerations imply that it exerts a radiation pressure force on the movable mirror,

$$F = \frac{2P}{c}, \tag{3.1}$$

where P is the incident power and c is the speed of light. With low enough losses in the cavity, and flexible enough mirrors, this minute force can lead to displacement

of the mirror which is measured via the light transmitted through the cavity.

This displacement of the mirror also leads to changing the resonance condition for the cavity. If the cavity length is increased, the cavity resonance moves to a longer wavelength. The optomechanical coupling constant g describes the resonance frequency change $\delta\omega$ with change in displacement δx.

$$g = \frac{\delta\omega}{\delta x}. \tag{3.2}$$

Outside of the basic concept of coupling mechanical and optical degrees of freedom, there have been many implementations. These implementations consist of both a multitude of platforms and additionally several different actuation mechanisms. These devices span in frequency from hertz to gigahertz and in mass from picogram to kilogram. I will present here a brief overview of several popular systems.

3.2 Optomechanical systems

3.2.1 Flexible mirror cavities

Optomechanical hysteresis in flexible mirror cavities suspended by wires are some of the pioneering experiments that heralded oscillations and cooling by radiation pressure optomechanics. These Fabry-Perot type cavities consist of a fixed mirror and a flexible mirror. Optical bi-stability due to radiation pressure in such a cavity had been demonstrated as early as 1983 (3). It was shown that radiation pressure from a 5 Watt laser on a small quartz plate (60 mg) suspended on tungsten wires was enough to cause a bistability.

In addition to bi-stability, this system has also been shown to optical cool the motion of a microlever. This cooling was demonstrated using a gold-coated silicon micro-cantilever as a mirror in one end of a Fabry-Perot cavity where the force was

due to photo thermal expansion and later on replaced by radiation pressure. The other cavity mirror is a semi transparent gold film coated on a cleaved fiber tip. The Brownian thermal motion of the cantilever mirror is opposed by a photo thermal force which is actively controlled by a servo loop (4).

3.2.2 Microtoroids

In 2005 microtoroids fabricated out of silica were shown to demonstrate radiation pressure induced mechanical vibrations (2). These microtoroids were fabricated on-chip in a silica on silicon process (5). They are coupled to via taped optical fibers (6; 7).

In this system, the centrifugal force exerted by light on the toroid walls as it circulates induces a mechanical flex on the structure supporting the toroid. The mechanical flexing changes the optical path length of the resonator and brings the incident light off resonance. Once off resonance, the structure relaxes allowing the process to repeat. This oscillation occurs at the eigenmechanical frequency of the structure. For 100 micron scale diameters, oscillation rates are in the MHz range. Higher frequencies have been obtained using higher order mechanical modes (8). Optomechanical chaose was demonstrated when gain and loss was further increased (9).

Researchers have also demonstrated resolved sideband cooling of microtoroids (10). To accomplish this, an optical resonance is pumped at its lower sideband. The linewidth of the optical resonance is many times narrower than the mechanical frequency. As the optical sidebands from the mechanical modulation are outside of the linewidth of the original optical resonance it is referred to as resolved sideband. A microtoroid which was pre-cooled to a thermal occupancy of 200 quanta (600 mK), was cooled to an average occupancy of 9 via resolved sideband cooling (11).

In 2005, it was predicted that the optical gradients in whispering gallery resonators could induce optical forces (12). This led to another novel take on the microdisk sys-

tem: the demonstration of mechanical actuation and cooling using the optical gradient force (13). This takes a double-disk structure made of two silica microdisks stacked on top of each other with a nanoscale gap in between. As the gap in between is very small and the mechanical motion is across the gap, the per photon optomechanical coupling rate is very large (13).

3.2.3 Thin membranes

Thin membranes placed in a Fabry-Perot cavity combine the benefits of high quality optical cavities with low mechanical mass (14). These membranes in the middle cavities offer finesses of 10^5. The membranes are around 50 nm thick and vibrate at 300 kHz rates (14). Another benefit is the double cavity allows cavity detuning to be a quadratic function of the membrane position. This has been predicted to allow a quantum non-demolition phonon number readout of the membrane (15).

3.2.4 Brillouin optomechanics

I will present the introduction of Brillouin scattering as an optomechanical actuation mechanism in micro devices (16). Brillouin scattering is the interaction of light with a density variation. Previous optomechanical actuation mechanism have been based on the scattering force, where light exerts force based on its linear momentum (2), or the gradient force, where a center of mass is pulled in the direction of an electric field gradient (13). Here, an electrostrictive force increases the density of material in regions of high electric field. We comment that while all of these forces originate from the Maxwell stress tensor that provides the mechanical stress at each point as it originates from electromagnetic momentum conservation considerations, the names "gradient force," "scattering force," and "electrostrictive force," are common to distinguish between different platforms (17). This causes a scattering of light as there is a change in refractive index with increased density. I will show in the

following chapters how this process can be used to excite a large range of frequencies of mechanical motion. I will further theoretically and experimentally demonstrate its ability to cool a mechanical mode. This is the first micro platform in which light sound interaction is demonstrated. It relies on three resonance enhancement and obtains high frequency irrespective of device size. The acoustical wavelength is half of the optical wavelength in the medium and allows mechanical vibration rates of 11 GHz.

REFERENCES

[1] V. Braginsky, A. Manukin, and M. Tikhonov, "Investigation of dissipative ponderomotive effects of electromagnetic radiation.," *Sov. Phys. JETP*, vol. 31, pp. 829–830, 1970.

[2] T. Carmon, H. Rokhsari, L. Yang, T. J. Kippenberg, and K. J. Vahala, "Temporal Behavior of Radiation-Pressure-Induced Vibrations of an Optical Microcavity Phonon Mode," *Phys. Rev. Lett.*, vol. 94, p. 223902, June 2005.

[3] A. Dorsel, J. McCullen, P. Meystre, E. Vignes, and H. Walther, "Optical Bistability and Mirror Confinement Induced by Radiation Pressure," *Physical Review Letters*, vol. 51, no. 17, pp. 1550–1553, 1983.

[4] C. Metzger and K. Karrai, "Cavity cooling of a microlever," *Nature*, vol. 432, no. 7020, pp. 1002–1005, 2004.

[5] D. Armani, T. Kippenberg, S. Spillane, and K. Vahala, "Ultra-high-Q toroid microcavity on a chip," *Nature*, vol. 421, no. February, pp. 925–928, 2003.

[6] J. C. Knight, G. Cheung, F. Jacques, and T. a. Birks, "Phase-matched excitation of whispering-gallery-mode resonances by a fiber taper.," *Optics letters*, vol. 22, pp. 1129–31, Aug. 1997.

[7] M. Cai and K. Vahala, "Highly efficient hybrid fiber taper coupled microsphere laser.," *Optics letters*, vol. 26, pp. 884–6, June 2001.

[8] T. Carmon and K. J. Vahala, "Modal Spectroscopy of Optoexcited Vibrations of a Micron-Scale On-Chip Resonator at Greater than 1 GHz Frequency," *Physical Review Letters*, vol. 98, p. 123901, Mar. 2007.

[9] T. Carmon, M. Cross, and K. Vahala, "Chaotic Quivering of Micron-Scaled On-Chip Resonators Excited by Centrifugal Optical Pressure," *Physical Review Letters*, vol. 98, pp. 1–4, Apr. 2007.

[10] a. Schliesser, R. Rivière, G. Anetsberger, O. Arcizet, and T. J. Kippenberg, "Resolved-sideband cooling of a micromechanical oscillator," *Nature Physics*, vol. 4, pp. 415–419, Apr. 2008.

[11] R. Rivière, S. Deléglise, S. Weis, E. Gavartin, O. Arcizet, a. Schliesser, and T. J. Kippenberg, "Optomechanical sideband cooling of a micromechanical oscillator

close to the quantum ground state," *Physical Review A*, vol. 83, p. 063835, June 2011.

[12] M. Povinelli, S. Johnson, M. Lonèar, M. Ibanescu, E. Smythe, F. Capasso, and J. Joannopoulos, "High-Q enhancement of attractive and repulsive optical forces between coupled whispering-gallery- mode resonators.," *Optics express*, vol. 13, pp. 8286–95, Oct. 2005.

[13] Q. Lin, J. Rosenberg, X. Jiang, K. Vahala, and O. Painter, "Mechanical Oscillation and Cooling Actuated by the Optical Gradient Force," *Physical Review Letters*, vol. 103, pp. 1–4, Aug. 2009.

[14] a. M. Jayich, J. C. Sankey, B. M. Zwickl, C. Yang, J. D. Thompson, S. M. Girvin, a. a. Clerk, F. Marquardt, and J. G. E. Harris, "Dispersive optomechanics: a membrane inside a cavity," *New Journal of Physics*, vol. 10, p. 095008, Sept. 2008.

[15] J. C. Sankey, A. M. Jayich, B. M. Zwickl, C. Yang, J. G. E. Harris, and N. Haven, "Improved Position Squared Readout Using Degenerate Cavity Modes," in *Proceedings of the XXI International Conference on Atomic Physics*, (Singapore), pp. 1–19, World Scientic, 2008.

[16] M. Tomes and T. Carmon, "Photonic Micro-Electromechanical Systems Vibrating at X-band (11-GHz) Rates," *Physical Review Letters*, vol. 102, p. 113601, Mar. 2009.

[17] A. Cho, "Optics. Putting light's light touch to work as optics meets mechanics.," *Science (New York, N.Y.)*, vol. 328, pp. 812–3, May 2010.

CHAPTER IV

Brillouin Lasing in a Silica Microsphere

4.1 Introduction

High frequency mechanical oscillators are attractive as local oscillators. They can be used to support communication applications and atomic clocks where frequencies comparable with the Caesium transition (around 9GHz) are attractive. Increasing the vibration rate of a micro-electromechanical system is usually restricted limitations on its miniaturization. For instance, in cavities based on a moving cavity element such as in Figure4.1, the walls of an optical whispering gallery mode cavity (1), a flexible mirror in a Fabry-Perot, and a flexible membrane (2), frequency is restricted by the time it takes sound to cross these elements.

This condition can be relaxed by using higher order acoustical modes, which have multiple nodes along the direction of sound propagation. Using higher vibration rates will cause decreased efficiency as the higher order mechanical modes tend to leak into the support structures (3).

Another way to increase the order of the mechanical nodes while avoiding support structure losses is to use mechanical whispering gallery modes. In conventional MEMs devices, this would be accomplished by interdigitated metal electrodes which would induce a surface acoustic wave in a piezo electric material. Here, we take advantage of optical electrostriction to act as a virtual train of electrodes along the whispering

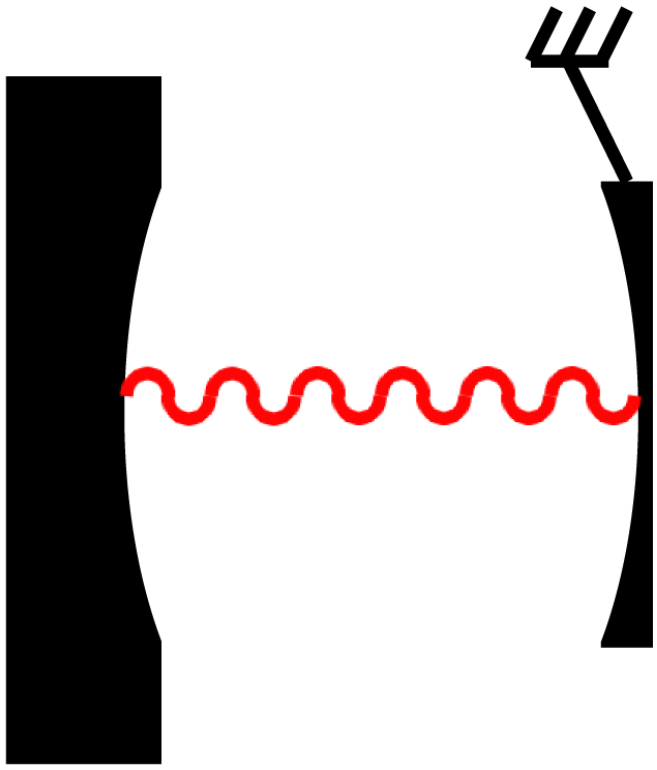

Figure 4.1: A Fabry-Perot cavity with a movable cavity element such as a mirror connected to a flexible spring can act as an optomechanical oscillator.

gallery circumference. This can be accomplished through stimulated Brillouin scattering. We replace traditional forces in photonic MEMS, such as centrifugal radiation pressure (1) that acts on the device walls, with stimulated Brillouin scattering (SBS) induced compression that acts on an acoustical density wave.

4.2 Optical and mechanical modes

For the demonstration of stimulated Brillouin scattering, we a take 100 to 200 μm silica sphere which allows optical and mechanical whispering gallery modes with very large azimuthal mode numbers (˜1000 nodes) to resonate. We calculate the mechanical whispering gallery mode using a finite element solver (COMSOL Multiphysics). Though the relevant mechanical modes are mostly longitudinal, our solver still accounts for transverse deformation occurring through the Poisson ratio. The optical mode is solved for following Mark Oxborrow's axsym code (4). An example optical and mechanical mode are presented in figures 4.2 and 4.3.

Only longitudinal mechanical modes having acoustical wavelength half of the optical wavelength are taken into account, as others modes are less likely to be excited by SBS (5; 6). Originating from momentum conservation, the acoustical wavelength is half the optical wavelength (5; 6), and the mechanical-mode area (in the plane transverse to propagation) is smaller than an optical-wavelength square (calculated in Figure 4.3). This allows the vibrating mass to be as low as 0.15 ng, which is much lighter than in prior photonic MEMS and allows low power consumption.

4.3 Brillouin scattering in microspheres

Knowing the forms of both the electromagnetic (Figure 4.2) as well as the acoustic WGM (Figure 4.3, we can discuss their opto-mechanical interaction. Brillouin scattering is the interaction of light with density variations. It is an inelastic scattering

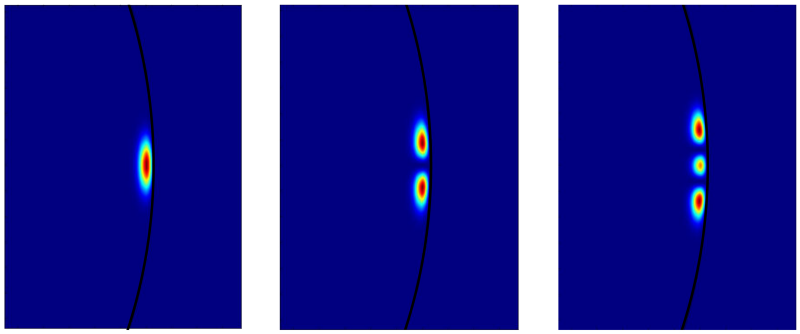

Figure 4.2: Example optical resonances for a 100 μm diameter silica sphere where color represents electric field. Resonances were solved for using Mark Oxborrow's axsym code (4).

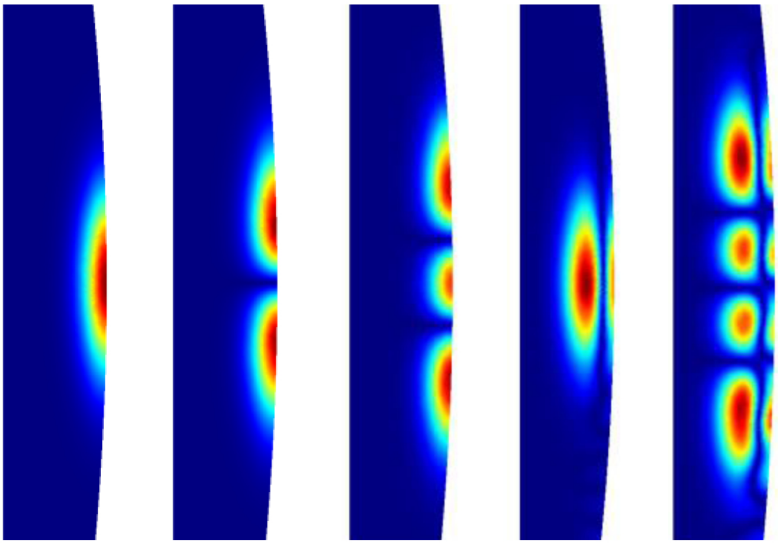

Figure 4.3: Example mechanical resonances for a 100 μm diameter silica sphere where color represents stress. Solved using a fully 3D solver in COMSOL Multiphysics using the structural mechanics module (7; 8).

process where the incident photon can either gain or lose energy depending on which way it is Doppler shifted. It is termed Stokes scattering if the photon gives up energy (red shift) and Anti-Stokes scattering if it receives energy (blue shift). Brillouin lasing in millimeter scale CaF2 whispering-gallery mode resonators has been reported (9).

In this process, a time-varying electric field gives rise to a time-varying electrostrictive strain. The presence of a local pressure in the resonator, on the other hand, changes the optical refractive index there. Hence, the mechanical vibration can cause exchange of energy between electromagnetic waves. The process is requires that the frequencies of the optical modes differ by an amount equal to the mechanical frequency to be efficient (5; 6). With sufficient pump intensity, the process can become stimulated. This means that with a single optical mode being pumped, both the second optical mode and the mechanical mode will be generated.

We first demonstrate stimulated Brillouin scattering in its traditional configuration. The pump optical mode is scattered into the counter propagating direction. In the case of a whispering gallery mode, this means the scattered mode is counter-circulating with the pump optical mode. We pump our system with light at angular frequency ω_p which is perfectly on resonance. The scattered optical mode is on resonance with a second optical mode and at angular frequency ω_s. In order for efficient generation of the scattered light, the mechanical angular frequency Ω_m must meet the following condition.

$$\Omega_m = \omega_p - \omega_s. \tag{4.1}$$

The pump excites the mechanical vibration through a self-consistent process in which the two optical modes beat, and via the electrostrictive effect, apply stress to the material which drives the mechanical mode. In return, this mechanical mode, via

the photo-elastic effect, writes a travelling optical grating that reflects and red Doppler shifts the optical pump into the Stokes mode. Such a self-consistent interaction where the vibration as well as the counter-circulating Stokes mode are produced by the one optical input only (10) is called stimulated Brillouin scattering. For satisfying phase match and for benefitting from resonance enhancement in such a process, both optical frequencies should be cavity resonances, and the separation between them should be equal to the mechanical resonance frequency as described by the following equation.

$$\omega_s = \omega_p(1 - \frac{vn}{c}), \tag{4.2}$$

where v is the velocity of sound and c/n is the speed of light. We approximate these velocities as that of plane waves and calculate them more accurately with the numerical WGM solvers as in figures 4.2 and 4.3. The resulting optical-mode separation given for silica at telecom wavelength (1.55 μm) is approximately 11 GHz. An additional requirement is that the integer number of optical wavelengths resonating along circumference must be twice the number of acoustical wavelengths. The first requirement ($\omega_s = \omega_p - \Omega_m$)is generally referred to as originating from energy conservation, while the second requirement originates from momentum conservation.

In fibers and bulk materials, propagation of the $\tilde{1}1$ GHz red-shifted Stokes light is guaranteed; however, in our micro-resonator, the approximately 300 GHz optical free spectral range restricts fundamental optical modes from being separated by 11 GHz. Luckily, using optical whispering gallery modes with high-order transverse profiles modifies the velocity of light. This recently allowed bringing optical modes very close to each other in frequency (11; 12). Thus, high-order optical modes can provide the required frequency separation of $\tilde{1}1$ GHz.

Further, we calculate that, analogous to the optical WGM (11; 12), the acous-

tical WGM can have high-order transverse profiles (Figure 4.3). This modifies the mechanical modes velocities, v, and hence also varies their frequencies. Thus, many mechanical modes are allowed, and the one with the $\Omega_m = \omega_p - \omega_s$ frequency will be excited. In our experiments, we observed resonators where almost every optical mode excites vibration, leading us to believe that the mechanical mode is selected from a continuity of modes.

As for required power, the stimulated Brillouin effect is analogous to stimulated Raman scattering with the mechanical mode playing the role of the molecular vibration (10). We can write the self-excitation threshold as

$$P_{threshold} = \left(\frac{\pi^2 n^2 V}{B g \lambda_p \lambda_s Q_p Q_s}\right)\left(\frac{1}{1 + Q_m \Lambda_m / 2\pi r}\right) \tag{4.3}$$

Here, $P_{threshold}$ denotes the incident power required to excite mechanical vibrations. V is the optical-mode volume and B stands for the modal overlap. The quality factors for the pump, stokes, and mechanical modes are $Q_{p,s,m}$. The wavelengths of the pump and stokes optical modes are $\lambda_{p,s}$ respectively, and the mechanical wavelength is Λ_m. The cavity radius is r is the cavity radius, and g is the nonlinear bulk Brillouin gain coefficient (6). The first fraction in Equation (4.3) is similar to the one known for the Raman threshold in cavities as described in (13). This first fraction includes the optical finesse (the number of times light recirculates the cavity) for the pump mode and describes the optical resonance enhancement via recirculations. High finesse is one important difference of our work from previous experiments, such as fibers resonators, which possess lower finesse and require higher power to excite SBS. The second fraction in Equation (4.3) stands for mechanical resonance enhancement by acoustical recirculations. In a large resonator where $r \gg Q_m \Lambda_m$, the second fraction is approximately one, describing no contribution of mechanical resonance

enhancement. In our case, the recorded mechanical dissipation for silica (6) gives a mechanical quality factor of 770. At our cavity size, this suggests a reduction of threshold by a factor of 2.3. As for competition from other processes, Brillouin gain g is considerably larger than the gain of other processes in silica (6) (e.g., Rayleigh and Raman scattering); it is hence expected that Brillouin gain will dominate with proper phase matching.

4.4 Experiment

Our experimental setup is shown in Figure 4.4. We use a 100 μm diameter spherical whispering gallery mode cavity (14) that is made out of a silica fiber via CO_2 laser reflow. The sphere exhibited an optical quality factor, Q_p, of 300×10^6 measured via the resonance width. Such spheres can also be made on-chip as described in (15). A pump laser is fiber coupled (16; 17) and thermally self locked (18) to an optical whispering gallery mode, providing the power to drive the mechanical whispering gallery mode. The signal is backward coupled while the pump is forward coupled as described in Figure 4.4. This is possible because the two modes circulate in opposite directions. We therefore have the freedom to measure each output (Stokes signal or pump transmission) separately.

4.4.1 Frequency

To showexcitation of mechanical modes in the X-band (11 GHz rates), we measure the frequency with an electrical spectrum analyzer. This is accomplished by taking the pump and Stokes light to a to a fast photodectector. The combination of the forward and backward outputs causes a beat note on the fast photodetector at the difference between the two frequencies. This beat note is sent to an electrical spectrum analyzer. The measured frequency is shown in Figure 4.5 and deviates only 2% from the numerically calculated frequencies for the mechanical mode. Such deviation is

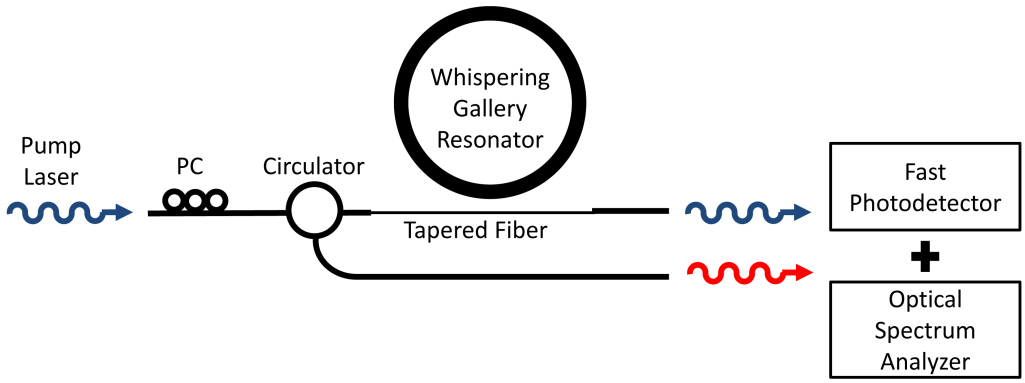

Figure 4.4: Experimental setup for measuring Brillouin scattering in silica whispering gallery resonators. Light is coupled into the whispering gallery resonator via a tapered fiber. The forward and backward scattered light is collected on both a fast photodetector and optical spectrum analyzer. The electrical signal from the fast photodetector is sent to an electrical spectrum analyzer. PC stands for polarization controller.

within the experimental error in measuring the size of our device. The width of this line is 0.7 MHz.

4.4.2 Optical Spectrum

In order to verify that this electrical signal is caused by the beat note between the pump and the Stokes scattered signal, we measure the optical spectrum of the back scattered light. Looking at the optical spectrum of the back scattered light reveals the Stokes scattered line as expected, and also the pump mode which is scattered backward by Rayleigh scattering in the resonator and residual scattering by both optical connectors. This is shown in Figure 4.6. The separation between the two lines is 11.5 GHz. This lies within the experimental error as our optical spectrum analyzer has a resolution limit of 1 GHz.

The Stokes line being stronger than back scattering from the pump indicates that the Rayleigh back scattering is at least 1 order of magnitude smaller than our scattering from mechanical vibration. This is expected as the Brillouin gain is larger

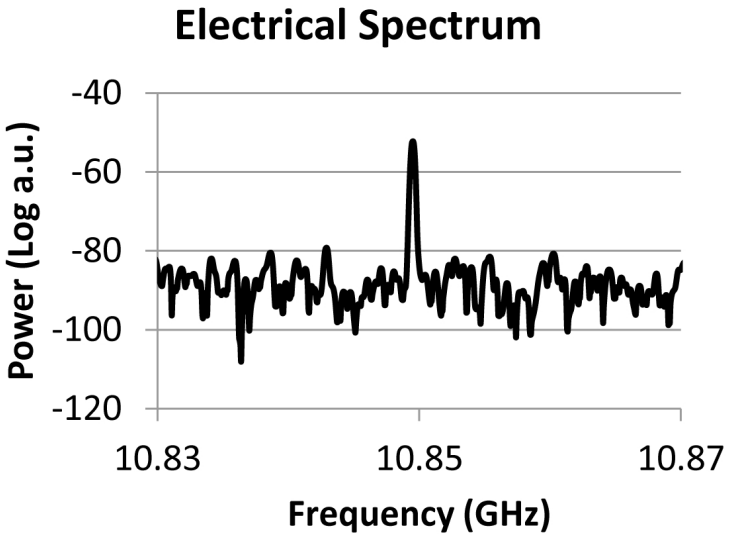

Figure 4.5: Beat note of the pump and Stokes scattered optical modes as captured by an electrical spectrum analyzer.

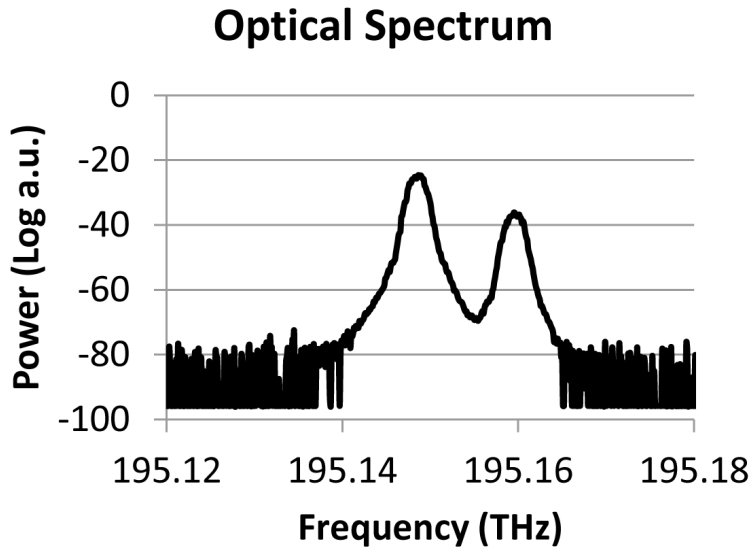

Figure 4.6: Optical spectrum of the back scattered light. The pump signal is on the right and the Stokes scattered light is on the left.

than the Rayleigh gain. Figure 4.6 also indicates that the Stokes line is more than 5 orders of magnitude stronger than the noise level in our system.

4.4.3 Efficiency and Threshold

The output power of the Stokes signal is measured with a power meter while varying the input power. The results are plotted in Figure 4.7. Experimental results indicate a slope efficiency of 90% and a 26 μW threshold. During measurement, part of the light is continuously monitored with an optical spectrum analyzer to verify that the cavity is clean from other optical effects.

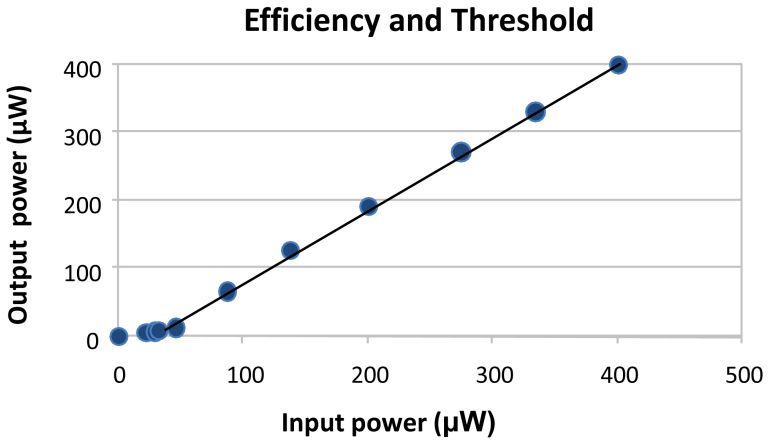

Figure 4.7: Light light curve showing threshold and slope efficiency. Experimental results indicate a slope efficiency of 90% and a 26 μW threshold.

4.4.4 Acoustical Mode Spectroscopy

Here, we used a 210 μm cavity, which has the advantage of allowing hundreds of modes around 1011 GHz apart, each excited with a different optical wavelength. We move from one optical resonance to another by changing the laser wavelength, while recording the corresponding mechanical vibration frequency. The experimental results are given in Figure 4.8.

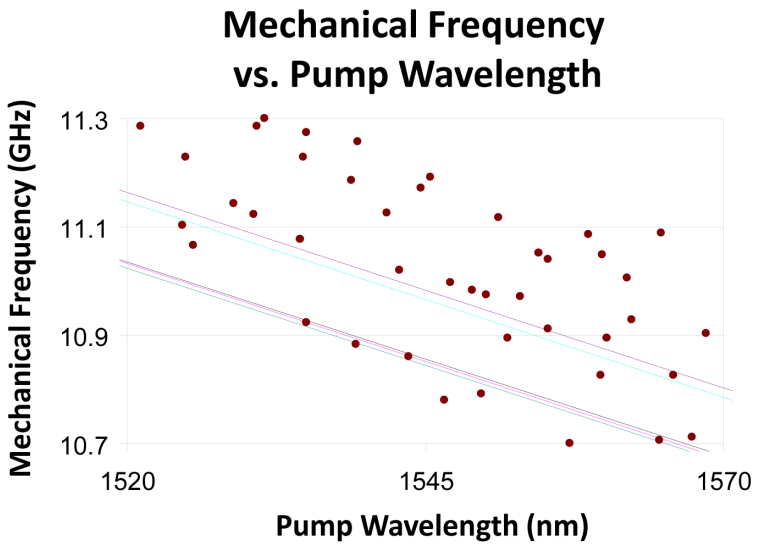

Figure 4.8: Plot of mechanical frequency versus pump wavelength. As the pump wavelength is increased, the mechanical frequency decreases as expected. The large variation in mechanical frequency at a given pump wavelength is potentially due to higher order mechanical modes.

The overall trend in Figure 4.8 is expected from the fact that the acoustical wavelength scales with the optical wavelength. One explanation for the variation in 4.8 can be the calculated abundance of high-order mechanical whispering gallery modes as shown in Figure 4.3. We note that in the past, the existence of such high-order optical modes was measured to relax phase match conditions and allow third-harmonic generation (19), making it likely that such mechanism exist also in the acoustical domain. The fact that some of calculated high-order mechanical whispering gallery modes in Figure 4.3 better overlap spatially with a typical optical whispering gallery modes in Figure 4.2 makes it likely that these high-order mechanical whispering gallery modes explain the 400 MHz vibration frequency range for a given pump wavelength.

4.4.5 Cascaded Vibration Modes

In this experiment, we measure the optical spectrum at the forward and backward outputs. We measure that the opto-mechanical coupling in our system was strong

enough to excite up to three cascaded mechanical modes simultaneously as shown in Figure 4.9. This is accomplished with input power lower than 1 mW. Beat notes between such cascaded events should be approximately twice and three times the vibration rate (2×11 GHz and 3×11 GHz). As expected, we observe a beat note (between pump and the second Stokes line) at 22 GHz as shown in Figure 4.10. This is near the highest frequency that our electrical spectrum analyzer can measure.

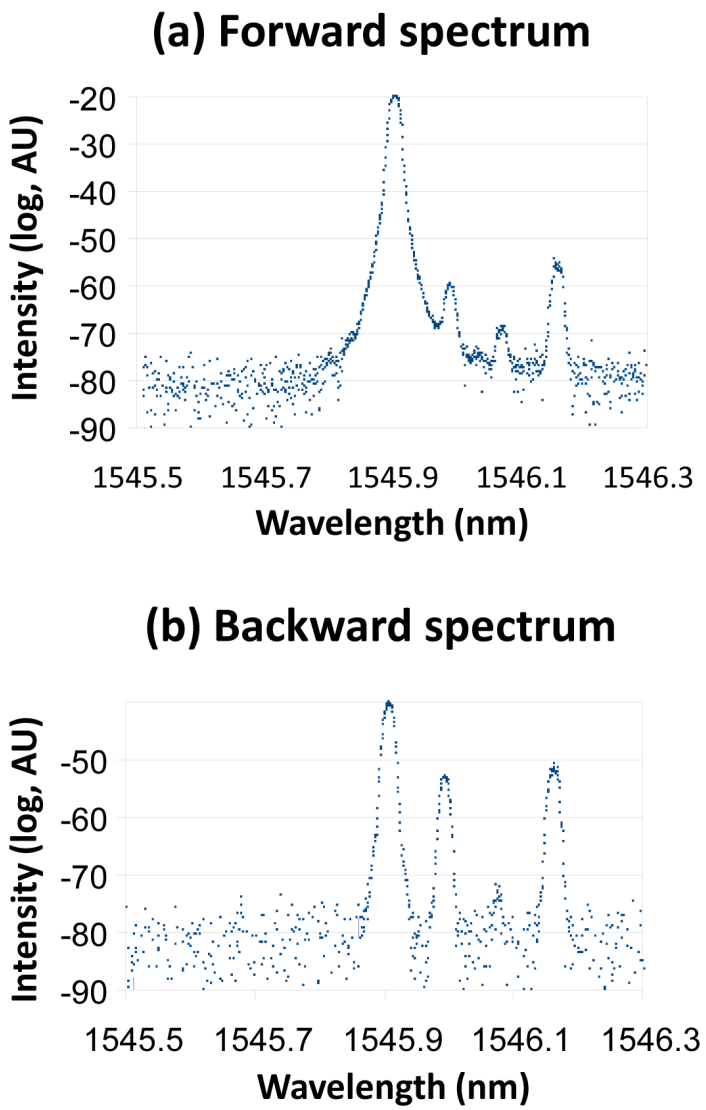

Figure 4.9: Optical spectrum of the forward scattered light (a) and backward scattered light (b) showing cascaded generation.

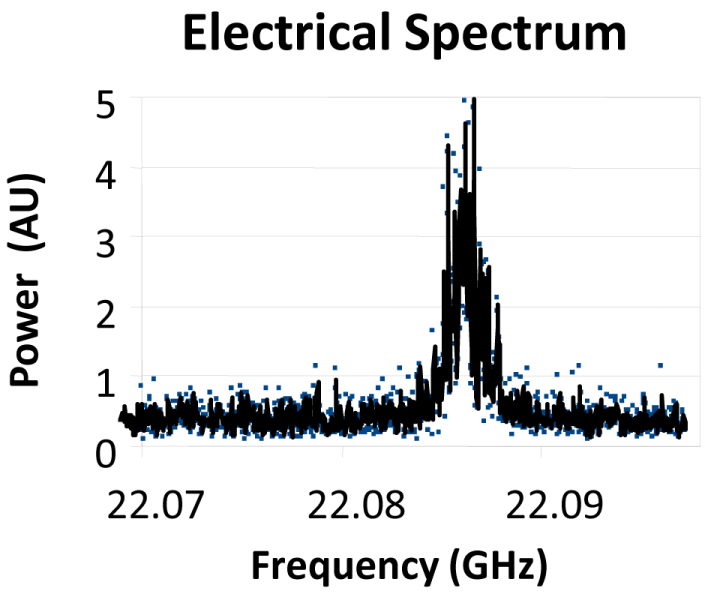

Figure 4.10: Electrical spectrum showing the beat note of the cascaded stimulated Brillouin scattering. The signal at 22 GHz corresponds to electrical beat note of the second generation of Brillouin scattering with the pump light.

4.5 Conclusion

We exploit stimulated Brillouin scattering to drive a high frequency mechanical whispering gallery mode in a silica resonator. Our device operates continuously in time at room temperature and pressure. The vibration is self-excited, and there is no need for external modulation or feedback. In contrast to previous photonic MEMS devices, we excite much higher frequencies. These frequencies scale inversely with optical wavelength. Additionally, unlike the breathing resonators where the Doppler shifted lines (1) were emitted together with the transmitted pump light, here, the Stokes and Pump signals are emerging from two separate fibers. This should enable future studies where detection of the Stokes line and the pump needs to be measured by seperate detectors.

Additionally, the vibration in our resonator is azimuthal, propagating around the equator. This contrasts with prior work where the vibration is along the radial direc-

tion (1; 3). Except for the geometrical difference, radial motion generally propagates toward the support and hence requires special mounting to prevent mechanical energy from leaking through the support.

In our work, the electric field of light drives vibration, replacing the electrical field applied by metal electrodes. We believe that the continuous trend in improving UV lasers and the availability of material with fast velocity of sound will allow future photonic MEMS devices based on stimulated Brillouin scattering to vibrate at even higher rates. Specifically, we predict that diamond would be an ideal candidate for extremely high frequency vibrations due to the currently available polishing techniques in crystals (20) which allow high-Q resonators. If pumped at the shortest transparent wavelength in Diamond, vibrations are predicted to be higher than 200 GHz rates. Though our device is different, high frequency oscillations were exploited to improve signal/noise ratio in various experiments (for example, (21; 22)), raising challenges such as making the measurement faster than phonon lifetime.

REFERENCES

[1] T. Carmon, H. Rokhsari, L. Yang, T. J. Kippenberg, and K. J. Vahala, "Temporal Behavior of Radiation-Pressure-Induced Vibrations of an Optical Microcavity Phonon Mode," *Phys. Rev. Lett.*, vol. 94, p. 223902, June 2005.

[2] J. D. Thompson, B. M. Zwickl, a. M. Jayich, F. Marquardt, S. M. Girvin, and J. G. E. Harris, "Strong dispersive coupling of a high-finesse cavity to a micromechanical membrane.," *Nature*, vol. 452, pp. 72–75, Mar. 2008.

[3] T. Carmon and K. J. Vahala, "Modal Spectroscopy of Optoexcited Vibrations of a Micron-Scale On-Chip Resonator at Greater than 1 GHz Frequency," *Physical Review Letters*, vol. 98, p. 123901, Mar. 2007.

[4] M. Oxborrow, "Traceable 2-D Finite-Element Simulation of the Whispering-Gallery Modes of Axisymmetric Electromagnetic Resonators," *IEEE Transactions on Microwave Theory and Techniques*, vol. 55, pp. 1209–1218, June 2006.

[5] A. Yariv, *Quantum electronics*. Wiley, 3 ed., 1989.

[6] R. W. Boyd, *Nonlinear optics*. Oxford, UK: Academic Press, 3rd ed., 2008.

[7] G. Bahl, X. Fan, and T. Carmon, "Acoustic whispering-gallery modes in optomechanical shells," *New Journal of Physics*, vol. 14, p. 115026, Nov. 2012.

[8] J. Zehnpfennig, G. Bahl, M. Tomes, and T. Carmon, "Surface optomechanics : calculating optically excited acoustical whispering gallery modes in microspheres," *Optics Express*, vol. 19, no. 15, pp. 14240–14248, 2011.

[9] I. S. Grudinin, A. B. Matsko, and L. Maleki, "Brillouin Lasing with a CaF_{2} Whispering Gallery Mode Resonator," *Physical Review Letters*, vol. 102, p. 043902, Jan. 2009.

[10] R. Chiao, C. Townes, and B. Stoicheff, "Stimulated Brillouin scattering and coherent generation of intense hypersonic waves," *Physical Review Letters*, vol. 12, no. 21, pp. 592–595, 1964.

[11] T. Carmon, H. G. L. Schwefel, L. Yang, M. Oxborrow, A. D. Stone, and K. J. Vahala, "Static Envelope Patterns in Composite Resonances Generated by Level Crossing in Optical Toroidal Microcavities," *Physical Review Letters*, vol. 100, p. 103905, Mar. 2008.

[12] A. A. Savchenkov, A. B. Matsko, V. S. Ilchenko, D. Strekalov, and L. Maleki, "Direct observation of stopped light in a whispering-gallery-mode microresonator," *Physical Review A*, vol. 76, p. 23816, Aug. 2007.

[13] S. Spillane, T. Kippenberg, and K. Vahala, "Ultralow-threshold Raman laser using a spherical dielectric microcavity," *Nature*, vol. 415, pp. 621–623, 2002.

[14] D. W. Vernooy, V. S. Ilchenko, H. Mabuchi, E. W. Streed, and H. J. Kimble, "High-Q measurements of fused-silica microspheres in the near infrared," *Optics Letters*, vol. 23, no. 4, pp. 247–249, 1998.

[15] D. Armani, T. Kippenberg, S. Spillane, and K. Vahala, "Ultra-high-Q toroid microcavity on a chip," *Nature*, vol. 421, no. February, pp. 925–928, 2003.

[16] J. C. Knight, G. Cheung, F. Jacques, and T. a. Birks, "Phase-matched excitation of whispering-gallery-mode resonances by a fiber taper.," *Optics letters*, vol. 22, pp. 1129–31, Aug. 1997.

[17] M. Cai and K. Vahala, "Highly efficient hybrid fiber taper coupled microsphere laser.," *Optics letters*, vol. 26, pp. 884–6, June 2001.

[18] T. Carmon, L. Yang, and K. Vahala, "Dynamical thermal behavior and thermal self-stability of microcavities.," *Optics express*, vol. 12, pp. 4742–50, Oct. 2004.

[19] T. Carmon and K. Vahala, "Visible continuous emission from a silica microphotonic device by third-harmonic generation," *Nature Physics*, vol. 3, no. 6, pp. 430–435, 2007.

[20] V. Ilchenko, A. Savchenkov, A. Matsko, and L. Maleki, "Nonlinear Optics and Crystalline Whispering Gallery Mode Cavities," *Physical Review Letters*, vol. 92, p. 043903, Jan. 2004.

[21] R. Schoelkopf, P. Burke, a. Kozhevnikov, D. Prober, and M. Rooks, "Frequency Dependence of Shot Noise in a Diffusive Mesoscopic Conductor," *Physical Review Letters*, vol. 78, pp. 3370–3373, Apr. 1997.

[22] K. Schwab and M. Roukes, "Putting mechanics into quantum mechanics," *Physics Today*, no. July, pp. 36–42, 2005.

CHAPTER V

Brillouin Cooling

Brillouin scattering was predicted by Brillouin in 1922 and stimulated Brillouin scattering was predicted by Shen in 1963 (1). Brillouin scattering has always been thought of as a heating process where the signal increases with increasing pump power. In the case of cooling, the scattering light must absorb phonons and there will be a decrease in scattering. In order to enable cooling through scattering, the system must prefer scattering to bluer wavelengths. The Planck distribution however suggests that the system will prefer scattering to redder wavelengths. To combat this preference for heating, we use a microresonator in which the blue scattering is selectively resonantly enhanced compared to the red scattering that is off resonantly attenuated. We measure cooling from a reduction in the Brownian scattering when the input power is increased.

In this chapter, we analyze how to exploit Brillouin scattering of light from sound for the purpose of cooling opto-mechanical devices and present a quantum-mechanical theory for Brillouin cooling. Our analysis shows that significant cooling ratios can be obtained with standard experimental parameters. A further improvement of cooling efficiency is possible by increasing the dissipation of the optical anti-Stokes resonance.

5.1 Introduction

A major advantage of triply resonant optomechanical systems is the ability to provide resonant enhancement for both optical-pump and anti-Stokes light in addition to the mechanical mode (2) (Figure 5.1a). Such systems have been predicted to cool acoustical modes (3). Of particular interest is our recently demonstrated triply resonant system based on Brillouin scattering of light from sound (4; 5) as in Figure 5.1b. Brillouin scattering is relevant for all dielectrics and constitutes the strongest non-linearity in all of optics (6). It is less well know that Brillouin scattering can be used to cool by scattering photons in the anti-Stokes direction. Our recent experimental observation of such Brillouin cooling (7) suggests that a model is required to describe the potential of this new system for ground-state cooling (8; 9).

In light-sound interactions, light is scattered to both Stokes and anti-Stokes side bands, heating and cooling the system respectively. Selective excitation of side bands has been demonstrated in the past for ground-state cooling (10; 11). Here, in order to break the material heating-cooling symmetry, we study a resonator with an asymmetric resonance structure (12; 13). Figure 5.2a exemplifies our proposal to resonantly enhance the anti-Stokes process for cooling the mode, while at the same time off-resonantly attenuating the Stokes process to prevent heating. Obtaining a resonator that is proper for Brillouin cooling is challenging. This is because two optical resonances that have almost the same optical frequency but different propagation constants are needed in order to conserve both the energy and momentum which are given to light by the acoustical phonon.

One type of cavity that allows such optical-resonance pairs is whispering-gallery mode resonators (12; 13). In such resonators, the transverse (radial-polar) order of one mode can compensate for the frequency difference originating from the non-similar longitudinal (azimuthal) order of the other. This provides a pair of modes with different azimuthal wavevectors, but nearby frequencies, as experimentally observed

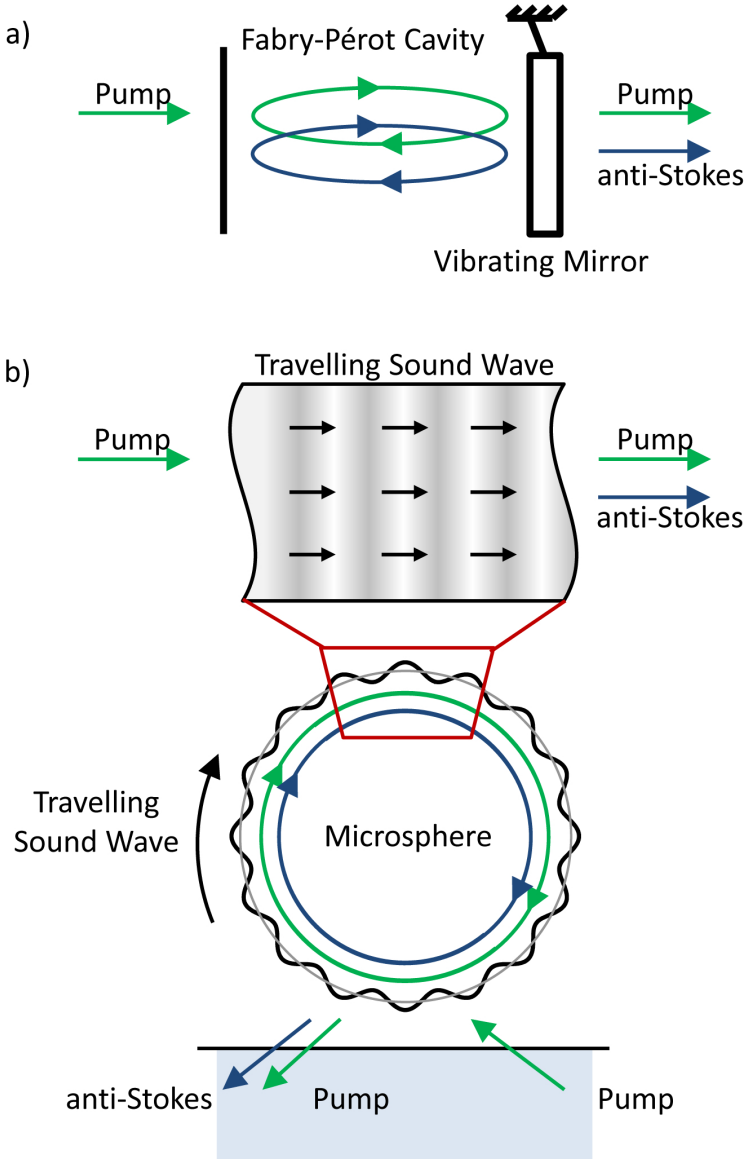

Figure 5.1: Triply resonant opto-mechanical systems. a) Radiation pressure couples two resonant optical modes to a mirror's mechanical resonance as proposed for cooling (3). b) Brillouin scattering of light by a sound wave photoelastically scatters pump light in the anti-Stokes direction as was recently experimentally demonstrated (7).

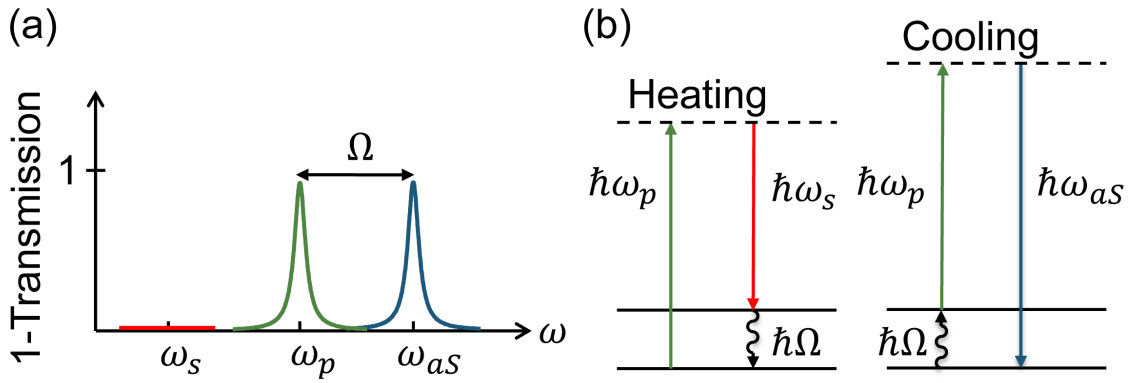

Figure 5.2: a) Sample resonator spectrum showing resonant enhancement possible at both pump and anti-Stokes frequencies, with attenuation at Stokes frequency. b) Energy diagram for Brillouin heating and cooling processes.

via the resulting stationary interference pattern (12; 13). The energy flow in Brillouin anti-Stokes cooling (4) that is analyzed here is opposite in respect to the Stokes excitation process (14; 15; 4). Additionally, cooling here is a spontaneous process.

5.2 Derivations of Brillouin Cooling

5.2.1 Derivation of Optoacoustic Coupling Rate

First we derive the optoacoustic coupling rate Γ_{opt} associated with Brillouin cooling. Consider a purely longitudinal density fluctuation that is propagating along a distance L through a cross-sectional area A_m. A displacement field u causes an elastic potential of $\frac{1}{2}A_m T(\partial_z u)^2$, where T is the spring constant per area. Additionally, the kinetic energy will be $\frac{1}{2}A_m \rho \dot{u}^2$ where ρ is the mass density. The interaction with the light field E is given by $\frac{1}{2}A_{opt}\gamma(\partial_z u)E^2$, where $\gamma = \rho\frac{\partial\epsilon}{\partial\rho}$ is the electrostrictive constant which relates a change in density to a change in permittivity, and A_{opt} is the area of the optical mode. The interaction area is taken to be the area of the optical mode as $A_{opt} \ll A_m$. Thus our Hamiltonian is of the form

$$\hat{H} = \int_0^L dz \left\{ \frac{\hat{\pi}^2(z)}{2\rho A_m} + \frac{A_m T}{2}(\partial_z \hat{u})^2 + \frac{A_{opt}\gamma}{2}(\partial_z \hat{u})\hat{E}^2 + ... \right\} , \tag{5.1}$$

where the omitted parts refer to the Hamiltonian of the electromagnetic field inside the medium. Here $\hat{\pi}(z) = A_m \rho \dot{\hat{u}}$ is the momentum density.

5.2.2 Quantization of the electromagnetic field and sound wave

For the electromagnetic field, consider a single polarization subjected to periodic boundaries. The electric field is of the form

$$\hat{E}(z) = \sum_k E_k \left[\hat{a}_k e^{ikz} + h.c. \right] , \tag{5.2}$$

where E_k is the zero-point amplitude of the electric field. Knowing the total energy of the electric and magnetic fields in free space, E^2 and B^2, to be $\frac{\hbar\omega_k}{4}$ per mode for the ground-state, we solve for the zero point fluctuation of the electric field.

$$E_k = \sqrt{(\hbar\omega_k)/(2A_{opt}L\epsilon)} . \tag{5.3}$$

Here ϵ is the material permittivity. Similar to the electric field, the longitudinal sound wave will be quantized in the following form

$$\hat{u}(z) = \sum_k u_k \left[\hat{b}_k e^{ikz} + h.c \right] . \tag{5.4}$$

Substituting Eq. (5.4) into Eq. (5.1) and solving for the coefficient of $\hat{b}_k\hat{b}_k^\dagger$ we obtain the expressions

$$u_k = \sqrt{(\hbar)/(2A_m L\rho\Omega_k)}\ , \tag{5.5}$$

where $\Omega_k = |k|v_s$ is the acoustic dispersion relation, and $v_s = \sqrt{T/\rho}$ is the speed of sound.

5.2.3 Acousto-optical interaction

Having derived expressions for both E_k and u_k we turn our attention to the optomechanical interaction term. Substituting expressions for E_k and u_k from Eqs. (5.2) and (5.4) into (5.1) and using the rotating wave approximation, the Hamiltonian simplifies to the following form

$$\begin{aligned}
\hat{H}_{optmech} &= \int_0^L dz(1/2)A_{opt}\gamma(\partial_z\hat{u})\hat{E}^2(z) \\
&= \frac{A_{opt}L\gamma}{2}\sum_{k,q} qu_qE_kE_{k+q}(\hat{b}_q + \hat{b}_{-q}^\dagger)(\hat{a}_{k+q}^\dagger\hat{a}_k + \hat{a}_k\hat{a}_{k+q}^\dagger) \\
&= \hbar\sum_{k,q} g_{k,q}(\hat{b}_q + \hat{b}_{-q}^\dagger)(\hat{a}_{k+q}^\dagger\hat{a}_k + \hat{a}_k\hat{a}_{k+q}^\dagger)\ ,
\end{aligned} \tag{5.6}$$

where $\hbar g_{k,q} = (1/2)A_{opt}L\gamma q u_q E_k E_{k+q}$.

The pump mode (p) is coupled to another optical mode (aS) and an acoustical mode in which energy conservation ($\omega_p = \omega_{aS} - \Omega$) and momentum conservation ($k_p = k_{aS} - q$) are fulfilled (4). Here, q and Ω represent the wavevector and frequency of the acoustical mode. Conservation of both quantities is possible in the kind of experimental setup studied here due to high order transverse optical modes (12; 13). Taking into account the momentum and energy conservation, the relevant coupling

term in $\hat{H}$ for this process will be:

$$\hbar g_{k,q}(\hat{b}_q \hat{a}^\dagger_{k+q} \hat{a}_k + h.c.) \ . \tag{5.7}$$

5.2.4 Solving the amplitude equations

As long as Brillouin cooling does not change the optical mode populations significantly, we can describe the interaction using coupled amplitude equations for the light field and the vibrational mode. As before with radiation pressure Hamiltonians (16), we can write a Hamiltonian for the laser-driven mode $\hat{a_p}$, the anti-Stokes mode $\hat{a_{aS}}$, and the phonon mode $\hat{b}$ of the form (written in a frame rotating at the laser frequency). Here Δ is the frequency mismatch between the driving laser and pump mode and δ_ω is the frequency difference between the pump and anti-Stokes optical modes.

$$\begin{aligned} \hat{H} = &-\Delta \hat{a}^\dagger_p \hat{a}_p - (\Delta - \delta\omega)\hat{a}^\dagger_{aS}\hat{a}_{aS} + \Omega \hat{b}^\dagger \hat{b} \\ &+ g(\hat{a}^\dagger_{aS}\hat{b}\hat{a}_p + \hat{a}_{aS}\hat{b}^\dagger \hat{a}^\dagger_p) + \hat{H}^{laser}_{drive} + \hat{H}_{diss} \ . \end{aligned} \tag{5.8}$$

This leads to the following classical equations for $\langle \hat{a_p} \rangle = \alpha_p$, $\langle \hat{a_{aS}} \rangle = \alpha_{aS}$, and $\langle \hat{b} \rangle = \beta$.

$$\dot{\alpha_p} = \left[i\Delta - \kappa_p/2 \right] \alpha_p + \kappa_p/2 \alpha^{max}_p - ig\alpha_{aS}\beta^* \ , \tag{5.9}$$

$$\dot{\alpha_{aS}} = \left[i\left(\Delta - \delta\omega\right) - \kappa_{aS}/2 \right] \alpha_{aS} - ig\alpha_p\beta \ , \tag{5.10}$$

$$\dot{\beta} = \left[-i\Omega - \Gamma/2 \right] \beta + \sqrt{n_{th}\Gamma}\xi(t) - ig\alpha_{aS}\alpha^*_p \ , \tag{5.11}$$

with $\langle \xi^*(t)\xi(t') \rangle = \delta(t - t')$. Here, α^{max}_p is the amplitude of the laser-driven mode

at resonance ($\Delta = 0$) in the absence of optomechanical coupling ($g = 0$), and n_{th} is the thermal phonon occupation at room temperature. We solve this system analytically in the simplified case where the laser-drive mode is on resonance, and the frequency difference between modes is chosen to be equal to the mechanical mode frequency Ω. Additionally, we assume a non-depleted pump and linearize the solution around $(\alpha_p, \alpha_{aS}, \beta) = (\alpha_p^{max}, 0, 0)$. Taking these simplifications into account, the equations to be solved reduce to:

$$\dot{\alpha_{aS}} = \left[-i\delta\omega - \kappa_{aS}/2\right]\alpha_{aS} - ig\alpha_p^{max}\beta \ , \tag{5.12}$$

$$\dot{\beta} = \left[i\Omega - \Gamma/2\right]\beta + \sqrt{n_{th}\Gamma}\xi(t) - ig\alpha_{aS}\alpha_p^{max*} \ . \tag{5.13}$$

We solve the system of equations in Fourier space to obtain an expression for $\langle|\beta(t)|^2\rangle = \bar{n}$ and $\langle|\alpha_{aS}(t)|^2\rangle = \bar{n}_{aS}$, the average phonon number and anti-Stokes photon occupation respectively.

$$\langle|\beta(t)|^2\rangle = -n_{th}\Gamma \left(\frac{|c_1|^2}{2Re[s_1]} + \frac{(c_1 c_2^*)}{s_1 + s_2^*} + \frac{(c_1^* c_2)}{s_1^* + s_2} + \frac{|c_2|^2}{2Re[s_2]}\right) \tag{5.14}$$

$$\langle|\alpha_{aS}(t)|^2\rangle = -g_{k,q}^2|\alpha_p^{max}|^2 n_{th}\Gamma \left(\frac{|c_3|^2}{2Re[s_1]} + \frac{(c_3 c_4^*)}{(s_1 + s_2^*)} + \frac{(c_3^* c_4)}{(s_1^* + s_2)} + \frac{|c_4|^2}{2Re[s_2]}\right) \tag{5.15}$$

$$s_{1,2} = -\left(\frac{\Gamma}{4} + \frac{\kappa}{4}\right) \pm \sqrt{\left(\frac{\Gamma}{4} - \frac{\kappa}{4}\right)^2 - g^2|\alpha_p^{max}|^2} \tag{5.16}$$

$$c_1 = \frac{s_1 + \frac{\kappa}{2}}{s_1 - s_2}, \ c_2 = \frac{s_2 + \frac{\kappa}{2}}{s_2 - s_1} \tag{5.17}$$

$$c_3 = 1/(s_1 - s_2), \ c_4 = 1/(s_2 - s_1) \tag{5.18}$$

5.2.5 Quantum noise approach

Alternatively, we can employ the quantum noise approach to derive the cooling and heating rates for the mechanical mode q subject to a situation where the mode k is assumed to be laser-driven and photons are scattered into the other mode $k+q$. In contrast to the amplitude equations discussed above, the rate equation approach will only work for $\kappa >> \Gamma_{opt} + \Gamma_M$, but unlike the amplitude approach it is not limited to situations where the optical mode populations remain essentially unchanged by the Brillouin processes. The idea will be to replace the driven photon mode operator by a c-number and to view the resulting Hamiltonian as composed of a fluctuating quantum noise term coupling to the mechanical mode. This quantum noise term essentially arises from the interference between the driven mode and the vacuum fluctuations in the second mode. Consider the mode k to be driven as $\hat{a}_k = \alpha e^{-i\omega_L t}$ where ω_L is the driving laser frequency. Upon substitution, the coupling term becomes:

$$\hbar g_{k,q}(\hat{b}_q \hat{a}_{k+q} \alpha e^{-i\omega_L t} + h.c.) \ . \tag{5.19}$$

where $\hat{b}_q$ couples to fluctuating quantum noise variable, $\hat{F} = \hbar g_{k,q} \hat{a}^\dagger_{k+q} \alpha e^{-i\omega_L t}$, in the form $\hat{H}_{int} = \hat{b}_q \hat{F}^\dagger + \hat{b}^\dagger_q \hat{F}$. The transition rate for phonon annihilation is:

$$\Gamma_{n-1\leftarrow n} = n \frac{1}{\hbar^2} \left\langle \hat{F}\hat{F}^\dagger \right\rangle_{\omega=\Omega} \ , \tag{5.20}$$

$$\left\langle \hat{F}\hat{F}^\dagger \right\rangle_{\omega} = (\hbar g_{k+q})^2 \bar{n}_{phot} \ 2Re\left[\frac{-1}{i(\Delta+\omega) - \kappa/2}\right] \ . \tag{5.21}$$

Likewise, the transition rate for phonon creation is

$$\Gamma_{n\leftarrow n-1} = n\frac{1}{\hbar^2}\left\langle \hat{F}^\dagger \hat{F}\right\rangle_{\omega=-\Omega} \ , \tag{5.22}$$

$$\left\langle \hat{F}^\dagger \hat{F}\right\rangle_{\omega} = \int dt\ e^{-i\omega t}\left\langle \hat{F}^\dagger(t)\hat{F}(0)\right\rangle = 0 \ . \tag{5.23}$$

Taking into account both transition rates, we are left with a cooling rate that is set by the balance between up- and downward transitions. It can be written in the form:

$$\Gamma_{opt} = \Gamma_0 \bar{n}_{phot} \ , \tag{5.24}$$

$$\Gamma_{opt} = g_{k+q}^2 \frac{\kappa}{(\kappa/2)^2 + (\omega_{k+q} - \omega_L - \Omega)^2} \ , \tag{5.25}$$

where Γ_{opt} quantifies the rate of Brillouin scattering. Here we have split off the dependence on the photon number $\bar{n}_{phot}$ circulating inside the lower optical mode. Below, we will display the slightly generalized expressions for the average up- and down-transition rates (deduced from Eqs. (5.20) and (5.22)) for the case of arbitrary photon numbers in both optical modes.

5.2.6 Rate equation approach

We can now proceed to solve a system of rate equations to determine the average phonon number in our system. We note that these rate equations do not take into account non-resonant scattering processes (scattering into the tails of the optical density of states, suppressed by a factor $(\kappa/\Omega)^2$) and would also cease to be valid in a strong coupling regime (where $\Gamma_{opt} > \kappa, \Omega$). Having derived the form of Γ_{opt}, let us now consider a two level optical system with photon decay rates κ_p and κ_{aS} for the pump and anti-Stokes modes respectively. The transition rates between the two levels

will be written in terms of the optomechanical coupling rate Γ_0, the average photon occupations of the two optical states $\bar{n}_p$ and $\bar{n}_{aS}$, and the average phonon occupation $\bar{n}$. The up transition corresponds to cooling and the down transition to heating.

$$\Gamma_\uparrow = \Gamma_0 \bar{n}_p(\bar{n}_{aS}+1)\bar{n} \ , \tag{5.26}$$

$$\Gamma_\downarrow = \Gamma_0(\bar{n}_p+1)\bar{n}_{aS}(\bar{n}+1) \ . \tag{5.27}$$

We can write the rate equations for the two levels based on the cavity decay rates and the heating and cooling transition rates, and the steady state photon number due to the driving laser $\bar{n}_p^L$.

$$\dot{\bar{n}}_{aS} = -\bar{n}_{aS}\kappa_{aS} - \Gamma_\downarrow + \Gamma_\uparrow \ , \tag{5.28}$$

$$\dot{\bar{n}}_p = (\bar{n}_p^L - \bar{n}_p)\kappa_p + \Gamma_\downarrow - \Gamma_\uparrow \ , \tag{5.29}$$

$$\dot{\bar{n}} = (\bar{n}_{th} - \bar{n})\Gamma_M + \Gamma_\downarrow - \Gamma_\uparrow \ . \tag{5.30}$$

Solving for the steady state solution by setting the time derivatives equal to zero yields a set of equations which relate the photon occupations to the pump laser and acoustical phonon occupation.

$$\bar{n}_p = \bar{n}_p^L - (\Gamma/\kappa_p) \ , \tag{5.31}$$

$$\bar{n}_{aS} = (\Gamma/\kappa_{aS}) \ , \tag{5.32}$$

$$\Gamma \equiv \Gamma_\uparrow - \Gamma_\downarrow = (\bar{n}_{th} - \bar{n})\Gamma_M \ . \tag{5.33}$$

We see that $\Gamma = \Gamma[\bar{n}, \bar{n}_p(\bar{n}), \bar{n}_{aS}(\bar{n})]$ is a nonlinear function of $\bar{n}$. Thus we must solve the following relation,

$$\Gamma(\bar{n}) = (\bar{n}_{th} - \bar{n})\Gamma_M \ , \tag{5.34}$$

where $\bar{n}$ will be a function of the dimensionless parameters $\bar{n}_{th}, \bar{n}_p^L, \frac{\kappa_p}{\Gamma_M}, \frac{\kappa_{aS}}{\Gamma_M}, \frac{\Gamma_0}{\Gamma_M}$.

5.3 Discussion

In the simple limit where the optical relaxtion rates κ_p, κ_{aS} are fast compared to the mechanical relaxation rate and optomechanical coupling rate Γ_0, Γ_M, we find only the cooling rate remains. In this case, the system simplifies to the following relations:

$$\Gamma_\downarrow = 0 \ , \qquad \Gamma_\uparrow = \Gamma_0 \bar{n}_p^L \bar{n} \ , \tag{5.35}$$

$$\bar{n}_p \approx \bar{n}_p^L \ , \qquad \bar{n}_{aS} \approx 0 \ , \tag{5.36}$$

$$\Gamma(\bar{n}) = \Gamma_\uparrow - \Gamma_\downarrow = \Gamma_0 \bar{n} \bar{n}_p^L \ , \tag{5.37}$$

$$\bar{n} = \bar{n}_{th} \frac{\Gamma_M}{\Gamma_M + \Gamma_0 \bar{n}_p^L} \ . \tag{5.38}$$

This is the usual classical cooling result where the cooling is unlimited with input power. We can also solve the full set of equations numerically and obtain the cooling rate as a function of input power. For the system, we take for example a 100μm diameter SiO_2 sphere (17; 7) such as the ones used in the context of Brillouin scattering previously (15; 4). The acoustical mode is taken to be a 50 MHz surface type mode like what was theoretically suggested (18), numerically calculated (19), and experimentally observed (4) to be excited via forward Brillouin scattering (20). The sphere is taken to have two optical modes of high quality factor $Q = 4\times10^8$. The optical modes are exactly separated by the mechanical oscillation frequency. Our pump is a telecom compatible source ($\lambda = 1.55\mu m$). The relevant area is taken to be

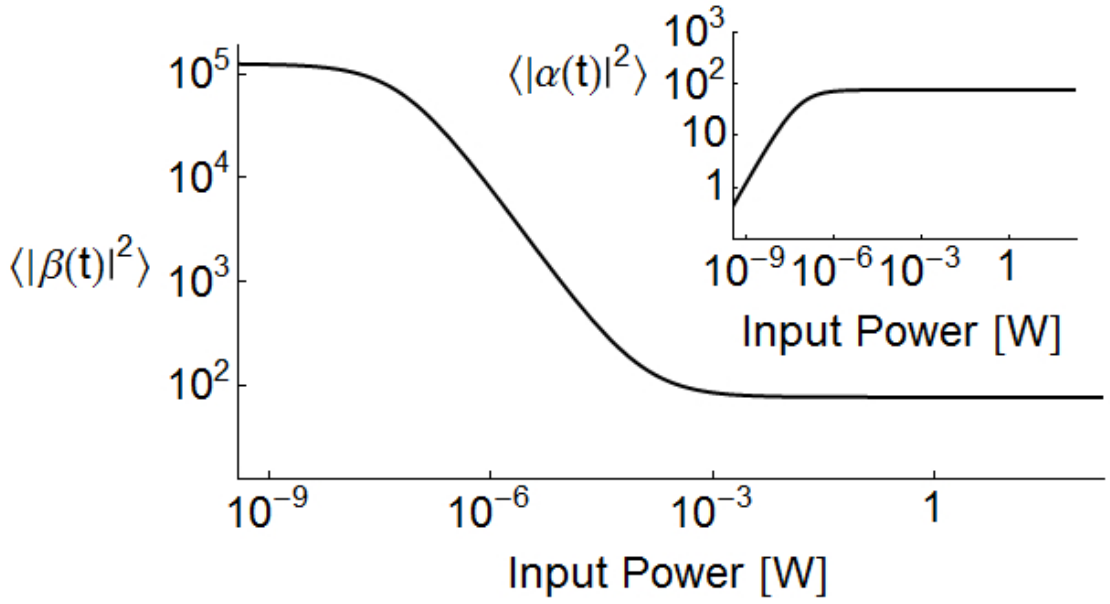

Figure 5.3: Average phonon number as a function of input power. The average phonon number starts from a thermal occupation of about 10^5 and cools by a ratio of about 1600. Inset: Intra-cavity anti-Stokes dependence on input power.

where the modes overlap, which is proportional to λ^2 (the optical mode area) (21) as the optical mode is much smaller than the acoustical one (19).

Figure 5.3 plots our theoretical prediction for the average phonon number in such a system as a function of input power. Significant cooling would begin at pump input powers of a few nW and saturates after a few mW. Starting from a room temperature phonon number of about 10^5 (as is typical for such systems), one could cool by a ratio of about 1600 in this example. As seen in the inset of Fig. 5.3, the amount of power circulating in the anti-Stokes mode clamps as the cooling process begins. As input power is increased, the final average phonon number asymptotically converges to a lower limit:

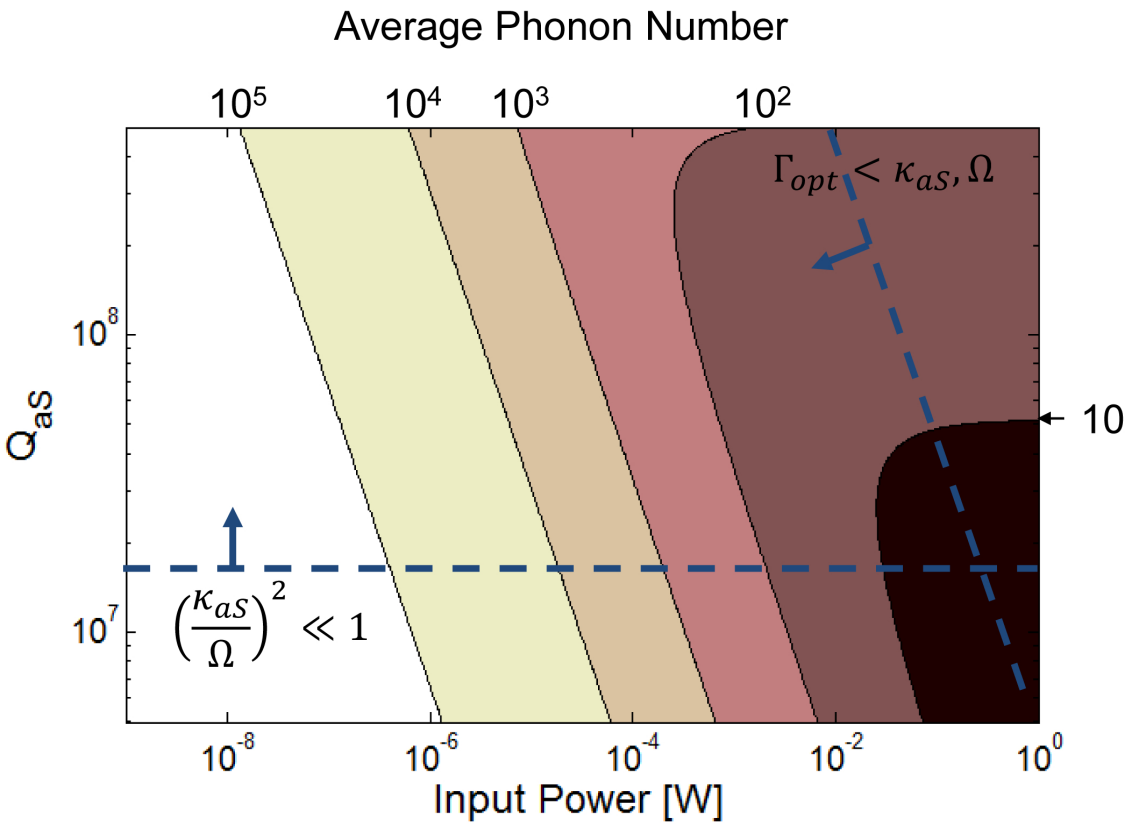

Figure 5.4: Average phonon number as a function of both input power and anti-Stokes quality factor. The dashed lines indicate the regime where our approximations hold.

$$n_{final} = \frac{n_{th}}{\frac{\kappa_{aS}}{\Gamma_M} + 1}. \tag{5.39}$$

Eq. (5.39) indicates that if the quality factor of the anti-Stokes resonance were deliberately lowered compared to the pump resonance, higher cooling ratios could be acheived: Brillouin cooling requires an efficient way to get rid of the anti-Stokes photons. We therefore determine the average phonon value as a function of both pump power and anti-Stokes mode quality factor, while all other parameters are left unchanged. Though many experimental challenges need to be overcome, as seen in Fig. 5.4, for diminished anti-Stokes quality factors, cooling ratios above 10^4 can be acheived.

5.4 Conclusion

We describe here a triply resonant structure for Brillouin cooling and develop the theory describing this system. Unlike before (22; 23; 24; 25; 26; 27; 28; 29), for Brillouin cooling, the Doppler reflector is a monotonically travelling acoustic wave. Additionally, different from fluorescent anti-Stokes cooling (30) that cools the whole thermal bath, Brillouin cooling evacuates heat from one selected vibrational mode, making it attractive for experiments in which this particular natural frequency is addressed (31). Brillouin scattering of light from sound is a member of a broad family of scattering processes that include Raman scattering. This raises the question whether Raman cooling of solids is possible in a similar manner despite the high rates involved.

REFERENCES

[1] Y. Shen and N. Bloembergen, "Theory of stimulated Brillouin and Raman scattering," *Phys. Rev*, vol. 137, no. 6A, pp. 1787–1805, 1965.

[2] C. Zhao, L. Ju, Y. Fan, S. Gras, B. Slagmolen, H. Miao, P. Barriga, D. Blair, D. Hosken, A. Brooks, P. Veitch, D. Mudge, and J. Munch, "Observation of three-mode parametric interactions in long optical cavities," *Physical Review A*, vol. 78, p. 023807, Aug. 2008.

[3] H. Miao, C. Zhao, L. Ju, and D. Blair, "Quantum ground-state cooling and tripartite entanglement with three-mode optoacoustic interactions," *Physical Review A*, vol. 79, p. 063801, June 2009.

[4] G. Bahl, J. Zehnpfennig, M. Tomes, and T. Carmon, "Stimulated optomechanical excitation of surface acoustic waves in a microdevice," *Nature Communications*, vol. 2, p. 403, July 2011.

[5] A. Savchenkov, A. Matsko, V. Ilchenko, D. Seidel, and L. Maleki, "Surface acoustic wave opto-mechanical oscillator and frequency comb generator.," *Optics letters*, vol. 36, pp. 3338–40, Sept. 2011.

[6] R. W. Boyd, *Nonlinear optics*. Oxford, UK: Academic Press, 3rd ed., 2008.

[7] G. Bahl, M. Tomes, F. Marquardt, and T. Carmon, "Observation of Spontaneous Brillouin Cooling," *ArXiv e-prints*, Sept. 2011.

[8] F. Marquardt, J. P. Chen, A. A. Clerk, and S. M. Girvin, "Quantum Theory of Cavity-Assisted Sideband Cooling of Mechanical Motion," *Physical Review Letters*, vol. 99, p. 093902, Aug. 2007.

[9] I. Wilson-Rae, N. Nooshi, W. Zwerger, and T. J. Kippenberg, "Theory of Ground State Cooling of a Mechanical Oscillator Using Dynamical Backaction," *Physical Review Letters*, vol. 99, p. 093901, Aug. 2007.

[10] G. Morigi, J. Eschner, and C. Keitel, "Ground state laser cooling using electromagnetically induced transparency," *Physical review letters*, vol. 85, pp. 4458–61, Nov. 2000.

[11] C. F. Roos, D. Leibfried, A. Mundt, F. Schmidt-Kaler, J. Eschner, and R. Blatt, "Experimental demonstration of ground state laser cooling with electromagnetically induced transparency.," *Physical review letters*, vol. 85, pp. 5547–50, Dec. 2000.

[12] T. Carmon, H. G. L. Schwefel, L. Yang, M. Oxborrow, A. D. Stone, and K. J. Vahala, "Static Envelope Patterns in Composite Resonances Generated by Level Crossing in Optical Toroidal Microcavities," *Physical Review Letters*, vol. 100, p. 103905, Mar. 2008.

[13] A. A. Savchenkov, A. B. Matsko, V. S. Ilchenko, D. Strekalov, and L. Maleki, "Direct observation of stopped light in a whispering-gallery-mode microresonator," *Physical Review A*, vol. 76, p. 23816, Aug. 2007.

[14] I. S. Grudinin, A. B. Matsko, and L. Maleki, "Brillouin Lasing with a CaF_{2} Whispering Gallery Mode Resonator," *Physical Review Letters*, vol. 102, p. 043902, Jan. 2009.

[15] M. Tomes and T. Carmon, "Photonic Micro-Electromechanical Systems Vibrating at X-band (11-GHz) Rates," *Physical Review Letters*, vol. 102, p. 113601, Mar. 2009.

[16] C. K. Law, "Interaction between a moving mirror and radiation pressure: A Hamiltonian formulation," *Physical Review A*, vol. 51, pp. 2537–2541, Oct. 1995.

[17] T. Carmon and K. J. Vahala, "Modal Spectroscopy of Optoexcited Vibrations of a Micron-Scale On-Chip Resonator at Greater than 1 GHz Frequency," *Physical Review Letters*, vol. 98, p. 123901, Mar. 2007.

[18] A. B. Matsko, A. A. Savchenkov, V. S. Ilchenko, D. Seidel, and L. Maleki, "Optomechanics with Surface-Acoustic-Wave Whispering-Gallery Modes," *Physical Review Letters*, vol. 103, p. 257403, Dec. 2009.

[19] J. Zehnpfennig, G. Bahl, M. Tomes, and T. Carmon, "Surface optomechanics : calculating optically excited acoustical whispering gallery modes in microspheres," *Optics Express*, vol. 19, no. 15, pp. 14240–14248, 2011.

[20] R. M. Shelby, M. D. Levenson, and P. W. Bayer, "Resolved Forward Brillouin Scattering in Optical Fibers," *Physical Review Letters*, vol. 54, no. 9, pp. 939–942, 1985.

[21] M. Oxborrow, "Traceable 2-D Finite-Element Simulation of the Whispering-Gallery Modes of Axisymmetric Electromagnetic Resonators," *IEEE Transactions on Microwave Theory and Techniques*, vol. 55, pp. 1209–1218, June 2006.

[22] C. Metzger and K. Karrai, "Cavity cooling of a microlever," *Nature*, vol. 432, no. 7020, pp. 1002–1005, 2004.

[23] D. Kleckner and D. Bouwmeester, "Sub-kelvin optical cooling of a micromechanical resonator.," *Nature*, vol. 444, pp. 75–8, Nov. 2006.

[24] S. Gigan, H. R. Böhm, M. Paternostro, F. Blaser, G. Langer, J. B. Hertzberg, K. C. Schwab, D. Bäuerle, M. Aspelmeyer, and A. Zeilinger, "Self-cooling of a micromirror by radiation pressure.," *Nature*, vol. 444, pp. 67–70, Nov. 2006.

[25] T. Carmon, H. Rokhsari, L. Yang, T. J. Kippenberg, and K. J. Vahala, "Temporal Behavior of Radiation-Pressure-Induced Vibrations of an Optical Microcavity Phonon Mode," *Phys. Rev. Lett.*, vol. 94, p. 223902, June 2005.

[26] T. Kippenberg, H. Rokhsari, T. Carmon, A. Scherer, and K. Vahala, "Analysis of radiation-pressure induced mechanical oscillation of an optical microcavity," *Physical review letters*, vol. 95, p. 033901, July 2005.

[27] H. Rokhsari, T. Kippenberg, T. Carmon, and K. Vahala, "Radiation-pressure-driven micro-mechanical oscillator," *Opt. Express*, vol. 13, no. 14, pp. 5293–5301, 2005.

[28] H. Rokhsari, T. Kippenberg, T. Carmon, and K. Vahala, "Theoretical and experimental study of radiation pressure-induced mechanical oscillations (parametric instability) in optical microcavities," *IEEE Journal of Selected Topics in Quantum Electronics*, vol. 12, pp. 96–107, Jan. 2006.

[29] M. Eichenfield, J. Chan, R. M. Camacho, K. J. Vahala, and O. Painter, "Optomechanical crystals.," *Nature*, vol. 462, pp. 78–82, Nov. 2009.

[30] R. Epstein and M. Sheik-Bahae, *Optical refrigeration: science and applications of laser cooling of solids*. Vch Pub, 2009.

[31] W. Marshall, C. Simon, R. Penrose, and D. Bouwmeester, "Towards Quantum Superpositions of a Mirror," *Physical Review Letters*, vol. 91, p. 130401, Sept. 2003.

CHAPTER VI

Tunneling From Microsphere

6.1 Introduction

Three centuries ago Newton reported on light transmission through a gap between prisms: a phenomenon that, much later, could be placed in the more general context of particle tunneling. As first described by Gamow (1), an alpha particle that does not have sufficient energy to climb over the nuclear potential, can, nonetheless, appear on the other side of the barrier; thereby escaping the nucleus as if it were digging a tunnel. Like these nuclear potentials (1), spherical dielectrics have a similar three dimensional [3D] potential for trapping light (2). Here, we directly image light propagating, without being seen, through the tunneling region of such an optical potential well. Images of the forbidden gap, as well as an interferogram showing wave-front spiraling, present a visual picture of the tunneling process.

Tunneling is universal to wave physics because it originates when an evanescent field transfers energy through a barrier to a region where a propagating wave is allowed. Tunneling has been reported for electrical currents (3), light (4; 5), sound (6), Bose-Einstein condensate (7), radio frequencies [RF] (8), and countless other physical phenomena. Studies in the optical domain include the question of tunneling velocity and superluminality (9), as well as energy leakage (10) from resonators. In the RF regime, wireless transfer of energy was recently demonstrated (11), benefiting

from the slow decay of the evanescent wave. When a wavefunction exits a potential by tunneling through the surrounding barrier (e.g. a spherical barrier), it is expected that the intensity will appear to emerge not from the device boundary, but instead from a region located at the other side of the potential barrier, which can be distant from the device physical boundary (2). Further, when leaving the barrier, the phase front can spiral as it propagates (12). Observations of these processes in real space are presented here.

As a brief review of the theory, spherical dielectrics can trap light (13; 14) inside in a potential well (Figure 6.1.b) near the surface. The energy can leave the well by tunneling through the centrifugal barrier that forms the outer wall of the potential well (2). The electric field for the resonant mode in a spherical trap is shown in Figure 6.2 and can be written in a spherical coordinate system as Equation (6.1) (2; 15):

$$\boldsymbol{E} \propto [\psi(kr)/kr][e^{i(m\phi-\omega t}]. \tag{6.1}$$

where the last term describes azimuthal propagation along the equator with m integer wavelengths resonating along the circumference at angular frequency ω. Here, k is the wavevector, and r, ϕ are radial and azimuthal coordinates respectively. As derived in (13; 14), $\psi(kr)$ obeys the reduced radial Schrodinger Equation (6.2),

$$-\frac{d^2\psi(r)}{dr^2} + V(r)\psi(r) = E\psi(r), \tag{6.2}$$

where the energy $E = k^2$, and where, for a dielectric sphere in free space, the potential is $V(r) = k^2(1 - n_{(r)}^2) + m(m+1)/r^2$ where $n_{(r)}$ is the refractive index (see Figure 6.1.b where the jump in radial potential at the dielectric-to-free-space interface is provided by the refractive index change from n to 1). Discussion of the similarities

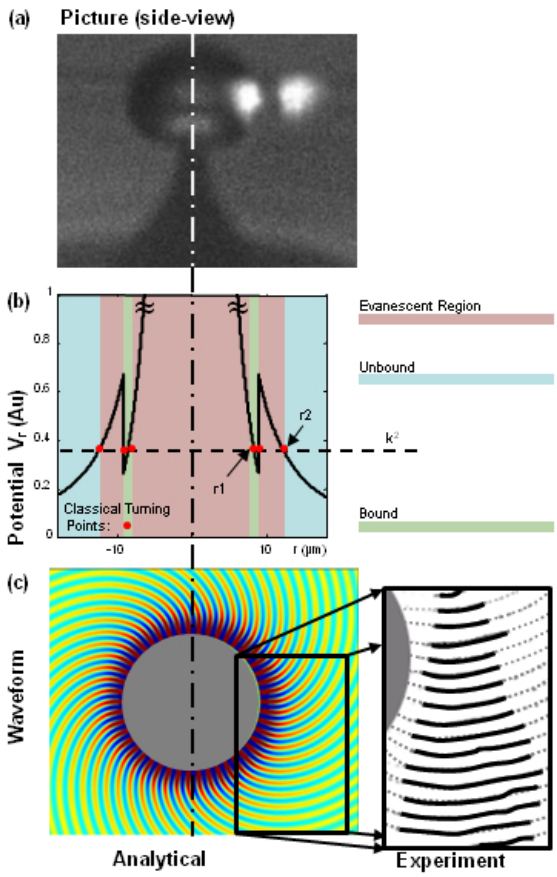

Figure 6.1: (a) Picture of light escaping the cavity. Light on the left marks the bound circulating mode via forward scattering. Light on the right is the unbound radiation after passing through the evanescent region without being seen. There are no objects or surfaces at the place where light emerges on the right. (b) Graph of spherical-resonator potential vs. radius in the equatorial plane. Colors indicate whether the region is bound, unbound, or evanescent. The radius of the sphere is a. (c) Calculation of waveform outside the cavity alongside experimental data. The dotted lines are a guide for the eye.

between the optical potential and the nuclear potential can be found in reference (2). A calculation presented in Figure 6.1.b shows how this potential implies an inner, classically-allowed well in the region $r1 < r < a$ (shown in green in Figure 6.1.b) where the energy is larger than the potential and the optical wave is bound. This region is surrounded by classically-forbidden regions ($E < V$) in which the wave is evanescent in the radial direction. The outer-most region is another, classically-allowed region, in which the photons, upon tunneling, radiate away from the sphere. The points where $E = V$ are called the classical turning points (2). From experimental view, these turning points affect both phase and intensity. The phase is expected transition from having only azimuthal propagation (within the outer turning point) to having also a radial component, forming a spiral (12). Measurable intensity is therefore expected to appear from a region after the most outer turning point leaving the tunneling region dark.

In the equivalent quantum-mechanical problem, a particle, such as the alpha particle, can spend time in the well and then tunnel through the classically forbidden region, $a < r < r2$ (shown in red in Figure 6.1.b), into the classically-allowed, free space (shown in blue in Figure 6.1.b), far from the sphere. Similarly, light can spend some time in the dielectric potential before tunneling out. During this time, intensity in this inner classically allowed region is enhanced by multiple-recirculation and has been used in the past to allow low-threshold lasing (17; 18), vibration by centrifugal- (19) and compression-pressure of light (20; 21), parametric oscillation (22), third-harmonic generation (23), and modal studies (24; 25). In such experiments, the tunneling rate is minimized by using relatively large dielectric diameters to support maximal recirculation and intensity enhancement.

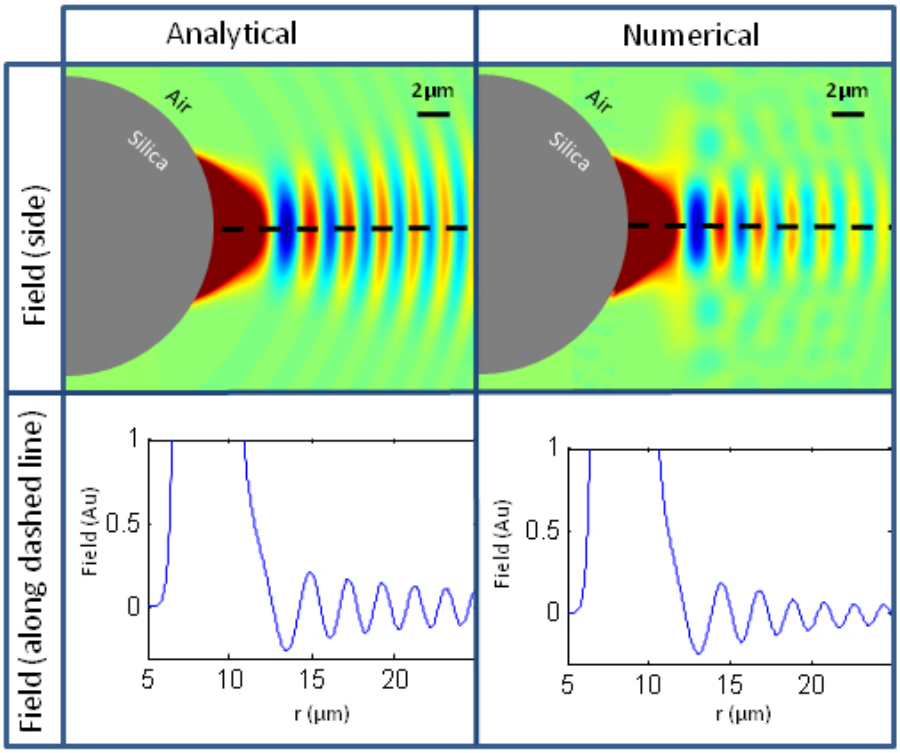

Figure 6.2: Top: Analytical, and numerical solution to the field outside of the cavity in a transverse plane. Numerical solution calculated via finite element method as described in (16). Bottom: The same field along the dashed line in the upper panels. A movie provided online shows that the field starts propagating radially only when crossing the outer turning point to the unbound region.

6.2 Experiment

Our experiment (Figure 6.1.a) uses optical whispering galleries fabricated of silica-on-a-silicon-chip (14), and the optical wavelength is 1.5 μm. Light is evanescently coupled into the cavity via a tapered fiber with greater than 99% efficiency (26). A side-view microscope with a 0.42 NA objective is used to image the emerging light as well as for mapping of the phase via interference with a plane-wave reference. The experiments were conducted with 1 mW of input power. The cavity quality factors varied from 10^5 to 10^7 depending on cavity diameter. Typically, more than 95% of this power was coupled into the resonator as evident by less than 5% of the power transmitted via the output coupler.

6.2.1 Phasefronts

Calculations of the tunneling radiation (2), reveal that the phase fronts begin to spiral only after leaving the outer turning point (Figure 6.1.c) (12). On the other hand, within that outer turning point, the phase fronts are flat planes passing through the origin of the dielectric. We measure this wavefront spiraling via interference with a reference plane wave. By moving a camera on a linear stage, we capture a series of images at different focal planes along the cavity side. In this manner an interferogram over a region outside of the external turning point is recorded and used to reconstruct the wavefront. Figure 6.1.c shows the processed experimental results alongside the analytical solution.

6.2.2 Intensity

The expected field intensity is calculated (Figure 6.2) and then an imaging integral(27) is performed in order to provide the image as seen by the camera (Figure 6.3.b). In more detail, the calculated cross sectional field (15; 16) is presented in Figure 6.2. In both the bound and evanescent regions extending far from the resonator boundary

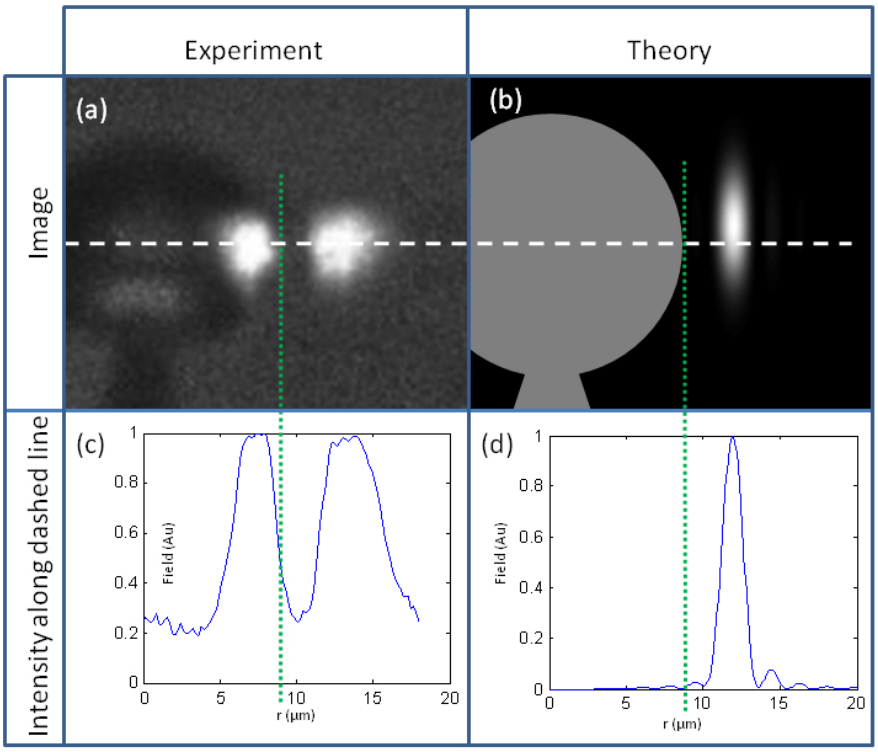

Figure 6.3: (a) Side-view image of cavity showing the internal mode scattering at the dielectric boundary (left spot) and also emitting at the edge of the tunnel barrier (right spot). Light is coupled to the cavity via a tapered fiber at the far edge of the cavity, hidden by the resonator and out of focus due to distance. We verified that no light is scattered from the taper alone by careful examination without a nearby resonator. (b) Calculation of the expected intensity distribution as would be imaged by the microscope (no surface scattering is assumed) (c) Intensity along the line shown in (a). (d) Intensity along the line shown in (b).

(marked by a dotted line), the field has no radial motion. As the radially standing electric field inside oscillates between positive and negative, a node is born at the boundary between the unbound and evanescent zones and starts to propagate radially in the unbound zone. The peaks past this point move away from the resonator in the unbound region, instead of oscillating in place as the field in the evanescent region does.

A side view photomicrograph of the cavity is presented in Figure 6.3.a. There are three important regions in the figure. Light circulating within the cavity is seen due to residual scattering at the dielectric interface. This scattering provides a convenient way to identify the physical boundary of the dielectric and therefore the inner, classical turning point. Light scattered from in the sphere is always present. Though some light is scattered in arbitrary directions, most of the light is Rayleigh scattered in the forward direction. This results in clock-wise circulating modes appearing on our camera (Figure 6.1.a) to scatter light from their right-hand side while the light scattered from the left-hand side is propagating away from our microscope and is not reaching our camera; this is in agreement with previous experimental results (23)]. As expected, changing the light to counter circulate caused the Rayleigh scattering (and the tunneling light) to switch to the other side in the image taken by the camera. While resonators containing fluorescent material emit light isotropically to produce an illuminated ring seen from all directions (18; 24; 25), our resonator is made of naked silica and produces mostly Rayleigh scattered light that can be viewed only from the forward side, (as in (23)). Beyond the cavity boundary in the micrograph, there is a dark region. This is the tunneling region. Finally, beyond the external classical turning point we see the emergence of light (out of thin air so to speak). As radiation from resonator is always propagating away from the resonator, it is not expected to be reflected from resonator. Reflection of the tunneled light and the Rayleigh scattered light were observed from the bottom silicon chip surface some 50

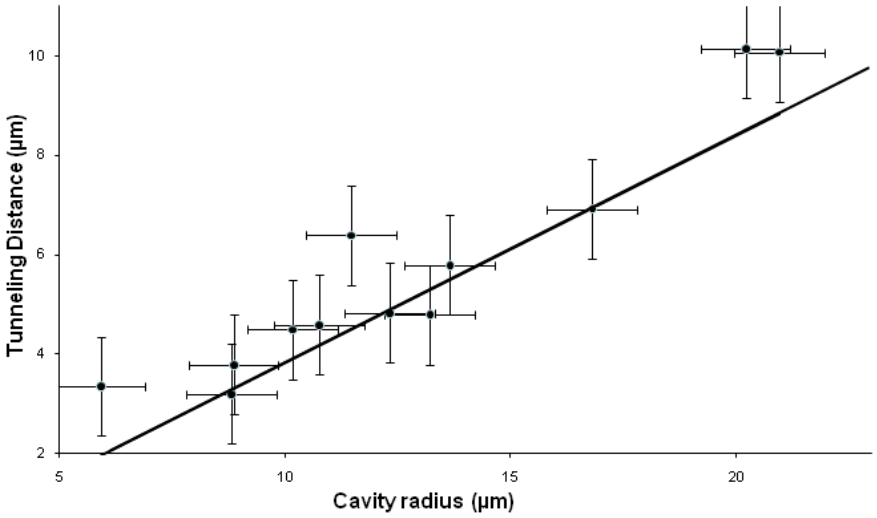

Figure 6.4: Plot of tunneling distance vs. cavity radius with experimental results as points and calculation as a line.

μm below and are out of the field of view in our images. The dark gap between the boundary of our device and the outer turning point is experimentally measured in Figure 6.3.a and calculated in Figure 6.3.c for comparison. Some deviation between the experimental and theoretical plots is believed to originate from the fact that the camera responsivity is not perfectly linear.

6.2.3 Tunneling Distance

To further verify the tunneling process, the effect of microcavity diameter on the tunneling gap is measured and compared with theory. Figure 6.4 shows the data plotted alongside a theoretically calculated line. The data show a roughly linear increase in tunneling distance with respect to cavity diameter. The largest tunneling distance measured is 10 μm, which is observed for a cavity of 20 μm in radius.

6.3 Conclusion

Circular resonators that were previously used in various applications (15; 28) have allowed direct observation of the forbidden tunneling region as well as the measurement of phase fronts beyond the outer, classical turning point. The observations are striking as light escaping the radial dielectric potential appears to emanate from nothing in a region far beyond the physical boundaries of the device.

REFERENCES

[1] G. Gamow, "Zur quantentheorie des atomkernes," *Zeitschrift f{ü}r Physik A Hadrons and Nuclei*, vol. 51, no. 3, pp. 204–212, 1928.

[2] B. R. Johnson, "Theory of morphology-dependent resonances: shape resonances and width formulas," *Journal of the Optical Society of America A*, vol. 10, p. 343, Feb. 1993.

[3] G. Binnig, H. Rohrer, C. Gerber, and E. Weibel, "Surface studies by scanning tunneling microscopy," *Physical review letters*, vol. 49, no. 1, pp. 57–61, 1982.

[4] A. Lewis, M. Isaacson, A. Harootunian, and A. Muray, "Development of a 500 spatial resolution light microscope:: I. light is efficiently transmitted through /16 diameter apertures," *Ultramicroscopy*, vol. 13, pp. 227–232, 1984.

[5] D. W. Pohl, U. C. Fischer, and U. T. Dürig, "Scanning near-field optical microscopy (SNOM)," *Journal of Microscopy*, vol. 152, no. 3, pp. 853–861, 1988.

[6] W. M. Robertson, J. Ash, and J. M. McGaugh, "Breaking the sound barrier: Tunneling of acoustic waves through the forbidden transmission region of a one-dimensional acoustic band gap array," *American Journal of Physics*, vol. 70, no. 7, pp. 689–693, 2002.

[7] C. Sias, a. Zenesini, H. Lignier, S. Wimberger, D. Ciampini, O. Morsch, and E. Arimondo, "Resonantly Enhanced Tunneling of Bose-Einstein Condensates in Periodic Potentials," *Physical Review Letters*, vol. 98, pp. 1–4, Mar. 2007.

[8] E. Ash and G. Nicholls, "Super-resolution aperture scanning microscope," *Nature*, vol. 237, pp. 510–512, 1972.

[9] H. G. Winful, "Tunneling time, the Hartman effect, and superluminality: A proposed resolution of an old paradox," *Physics Reports*, vol. 436, pp. 1–69, Dec. 2006.

[10] L. Vanshten, *Open resonators and open waveguides*. Golem Press, 2 ed., 1969.

[11] A. Kurs, A. Karalis, R. Moffatt, J. D. Joannopoulos, P. Fisher, and M. Soljacic, "Wireless power transfer via strongly coupled magnetic resonances.," *Science (New York, N.Y.)*, vol. 317, pp. 83–6, July 2007.

[12] G. Roll, T. Kaiser, S. Lange, and G. Schweiger, "Ray interpretation of multipole fields in spherical dielectric cavities," *Journal of the Optical Society of America A*, vol. 15, no. 11, p. 2879, 1998.

[13] D. W. Vernooy, V. S. Ilchenko, H. Mabuchi, E. W. Streed, and H. J. Kimble, "High-Q measurements of fused-silica microspheres in the near infrared," *Optics Letters*, vol. 23, no. 4, pp. 247–249, 1998.

[14] D. Armani, T. Kippenberg, S. Spillane, and K. Vahala, "Ultra-high-Q toroid microcavity on a chip," *Nature*, vol. 421, no. February, pp. 925–928, 2003.

[15] R. K. Chang and A. J. Campillo, *Optical processes in microcavities*, vol. 3. World Scientific Pub Co Inc, 1996.

[16] M. Oxborrow, "Traceable 2-D Finite-Element Simulation of the Whispering-Gallery Modes of Axisymmetric Electromagnetic Resonators," *IEEE Transactions on Microwave Theory and Techniques*, vol. 55, pp. 1209–1218, June 2006.

[17] S. Spillane, T. Kippenberg, and K. Vahala, "Ultralow-threshold Raman laser using a spherical dielectric microcavity," *Nature*, vol. 415, pp. 621–623, 2002.

[18] L. Yang, T. Carmon, B. Min, S. Spillane, and KJ, "Erbium-doped and Raman microlasers on a silicon chip fabricated by the solgel process," *Applied Physics*, vol. 86, 2005.

[19] T. Carmon, H. Rokhsari, L. Yang, T. J. Kippenberg, and K. J. Vahala, "Temporal Behavior of Radiation-Pressure-Induced Vibrations of an Optical Microcavity Phonon Mode," *Phys. Rev. Lett.*, vol. 94, p. 223902, June 2005.

[20] I. S. Grudinin, A. B. Matsko, and L. Maleki, "Brillouin Lasing with a CaF_{2} Whispering Gallery Mode Resonator," *Physical Review Letters*, vol. 102, p. 043902, Jan. 2009.

[21] M. Tomes and T. Carmon, "Photonic Micro-Electromechanical Systems Vibrating at X-band (11-GHz) Rates," *Physical Review Letters*, vol. 102, p. 113601, Mar. 2009.

[22] T. Kippenberg, S. Spillane, and K. Vahala, "Kerr-Nonlinearity Optical Parametric Oscillation in an Ultrahigh-Q Toroid Microcavity," *Physical Review Letters*, vol. 93, pp. 18–21, Aug. 2004.

[23] T. Carmon and K. Vahala, "Visible continuous emission from a silica microphotonic device by third-harmonic generation," *Nature Physics*, vol. 3, no. 6, pp. 430–435, 2007.

[24] T. Carmon, H. G. L. Schwefel, L. Yang, M. Oxborrow, A. D. Stone, and K. J. Vahala, "Static Envelope Patterns in Composite Resonances Generated by Level Crossing in Optical Toroidal Microcavities," *Physical Review Letters*, vol. 100, p. 103905, Mar. 2008.

[25] A. A. Savchenkov, A. B. Matsko, V. S. Ilchenko, D. Strekalov, and L. Maleki, "Direct observation of stopped light in a whispering-gallery-mode microresonator," *Physical Review A*, vol. 76, p. 23816, Aug. 2007.

[26] M. Cai and K. Vahala, "Highly efficient hybrid fiber taper coupled microsphere laser.," *Optics letters*, vol. 26, pp. 884–6, June 2001.

[27] B. E. A. Saleh and M. C. Teich, *Fourier Optics*, ch. 4, pp. 108–156. John Wiley & Sons, Inc., 1991.

[28] K. J. Vahala, "Optical microcavities," *Nature*, vol. 424, pp. 839–46, Aug. 2003.

CHAPTER VII

Other Work

In this chapter, I will discuss the other projects I have worked on during the course of my dissertation work.

7.1 Forward Brillouin scattering in microspheres

Owing to the higher order optical modes in microspheres (1; 2), light with nearly identical frequency, can propagate at significantly different phase velocities. This index of refraction difference between optical modes allows achieving phase match Brillouin scattering in the forward direction. We take advantage of this to excite mechanical vibrations with frequencies ranging from several MHz to a few GHz as seen in Figure 7.1. As opposed to the 11 GHz hypersonic frequencies required for backward Brillouin scattering in silica, these acoustical modes have high quality factor (44,000) and finesse of 900 (3). This work was reported in Nature Communications (3).

7.2 Observation of spontaneous Brillouin cooling

Recently, forward Brillouin scattering in microcavities has allowed access to low-frequency acoustical modes where mechanical dissipation is lower than optical dissipation, in accordance with the requirements for cooling. Here we experimentally

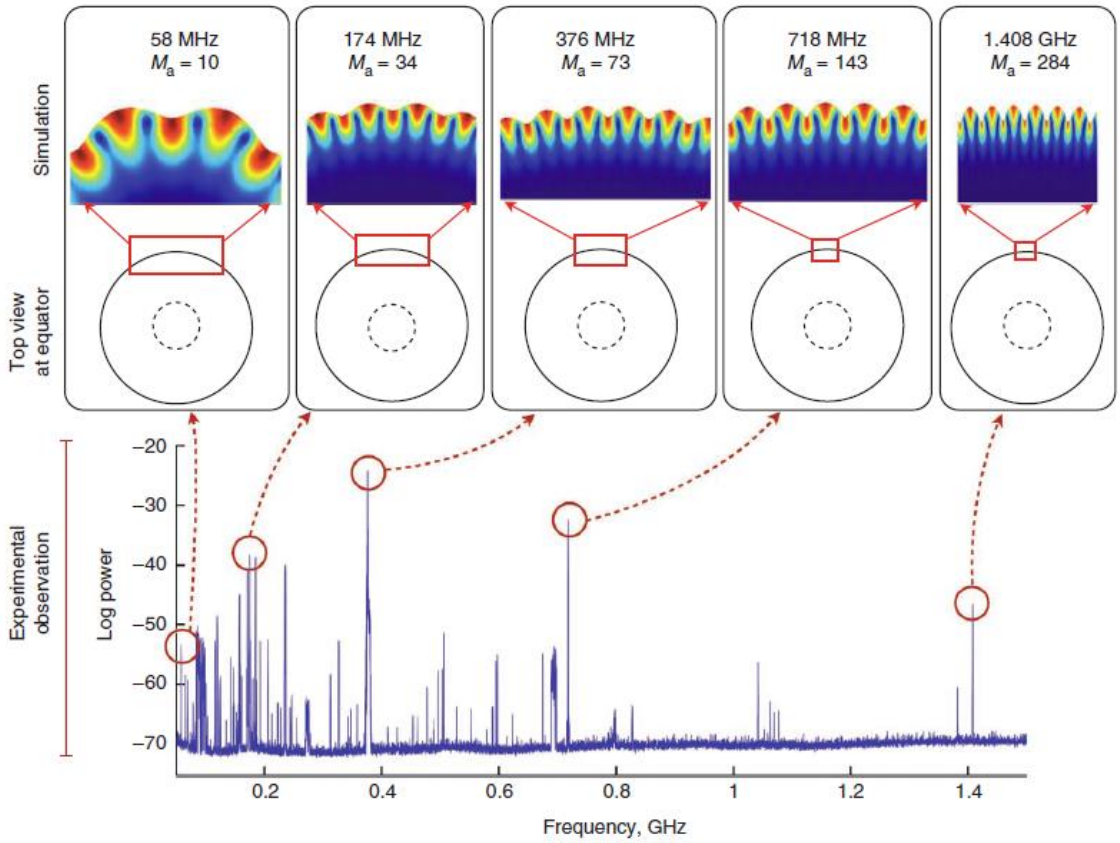

Figure 7.1: Phase matching is acheived for forward Brillouin scattering in silica microspheres. This allows excitation of acoustical modes at frequencies ranging from several MHz to a few GHz.

demonstrate cooling via such a forward Brillouin process in a microresonator (4). We show two regimes of operation for the electrostrictive Brillouin process: acoustical amplification as is traditional and an electrostrictive Brillouin cooling regime (Figure 7.2). Cooling is mediated by resonant light in one pumped optical mode, and spontaneously scattered resonant light in one anti-Stokes optical mode, that beat and electrostrictively attenuate the Brownian motion of the mechanical mode. This work was reported in Nature Physics (4).

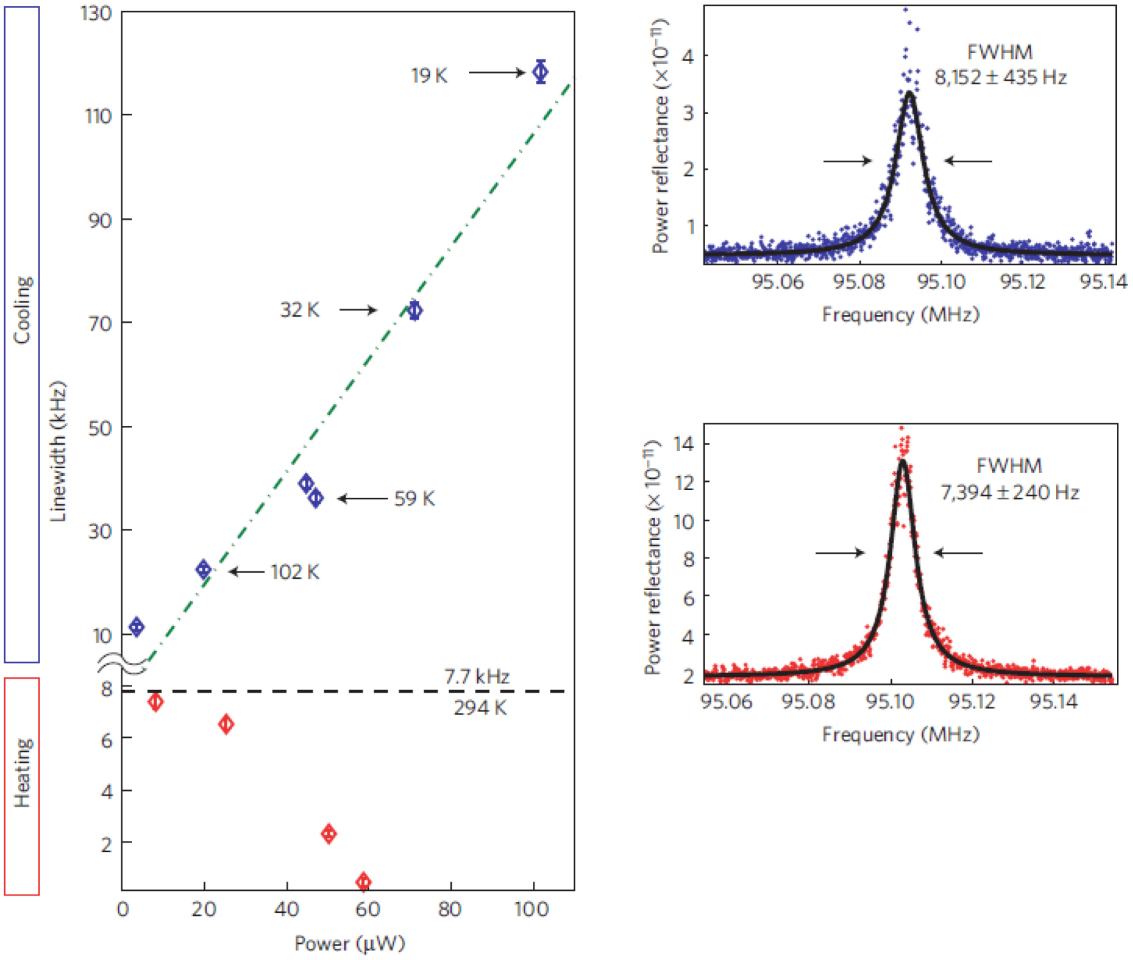

Figure 7.2: Measuring the linewidth of the electrical beat between the pump and anti-Stokes scattered optical modes allows determination of the effective mode temperature.

7.3 Acoustical mode families

Stimulated Brillouin scattering recently allowed experimental excitation of surface acoustic resonances in micro-devices, enabling vibration at rates in the range of 50 MHz to 12 GHz. The experimental availability of such mechanical whispering gallery modes in photonic-MEMS raises questions on their structure and spectral distribution. Here we calculate the form and frequency of such vibrational surface whispering gallery modes, revealing diverse types of surface vibrations including longitudinal, transverse, and Rayleigh-type deformations. We parametrically investigate these various modes by changing their orders in the azimuthal, radial, and polar directions to reveal different vibrational structures including mechanical resonances that are localized near the interface with the environment where they can sense changes in the surroundings.

We numerically study the mechanical modes of a silica microsphere (5). Multiple types of acoustical waves can be used to achieve phase matching in Brillouin optomechanics. While our original demonstration matches the frequency of a longitudinal sound wave, transverse and Rayleigh waves exist and travel at different velocities. Each of these families of sound waves has higher order transverse modes as seen in Figure 7.3. This work was reported in Optics Express (5).

7.4 Precession optomechanics

We propose a light-structure interaction that utilizes circularly polarized light to deform a slightly bent waveguide (6). The mechanism allows for flipping the direction of deformation upon changing the binary polarization state of light from $-\hbar$ to $+\hbar$. In this device, torque applied by spinning photons which are guided around a horizontal bend, causes mechanical deformation along the vertical direction. We name this effect precession optomechanics, since a photon in a waveguide and a precessing rotor will

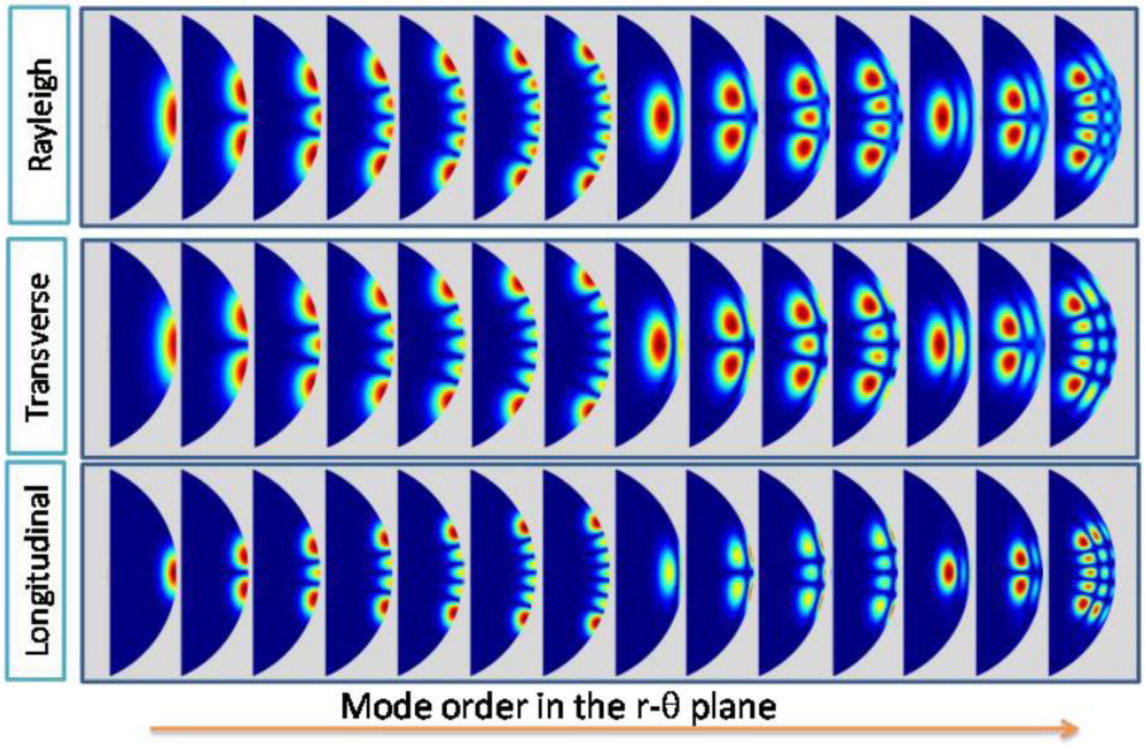

Figure 7.3: Multiple families of acoustical modes in a silica microsphere allow a broad set of phase matching conditions.

apply similar torque on what holds them when taking a similar turn. The expected deformation is depicted in Figure 7.4. This work was reported in Optics Express (6).

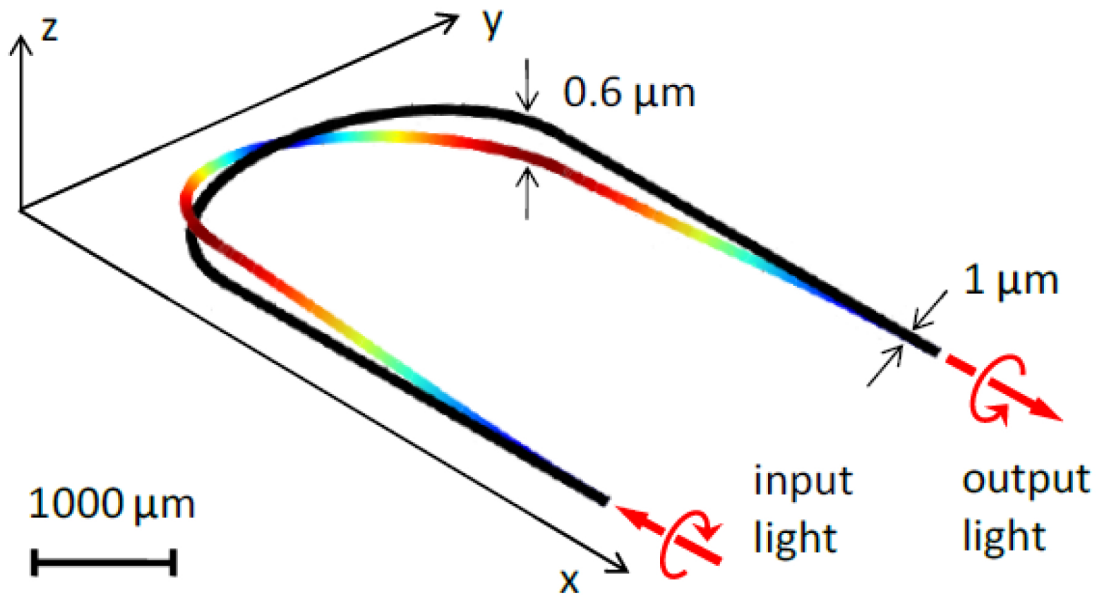

Figure 7.4: Illustration of the waveguide deformation due to the precession torque applied by photons.

7.5 Fourth harmonic generation in Lithium Niobate WGRs

We experimentally demonstrate continuous-wave ultraviolet emission through forth-harmonic generation in a millimeter-scale lithium niobate whispering-gallery resonator pumped with a telecommunication compatible infrared source (7; 8) as in Figure 7.5. The whispering-gallery resonator provides four spectral lines at ultraviolet, visible, near-infrared and infrared, which are equally spaced in frequency via the cascaded-harmonic process and span a 2-octave frequency band. Our technique relies on a variable crystal poling and high transverse order of the modes for phase-matching and a resonator quality factor of over 107 to allow cascaded-harmonic generation up to the fourth-harmonic at input pump powers as low as 200mW. The compact size of

the whispering gallery resonator pumped at telecommunication compatible infrared wavelengths and the low pump power requirement make our device a promising ultraviolet light source for information storage, microscopy, and chemical analysis. This work was reported in Applied Phsyics Letters (8) and Optics Express (7).

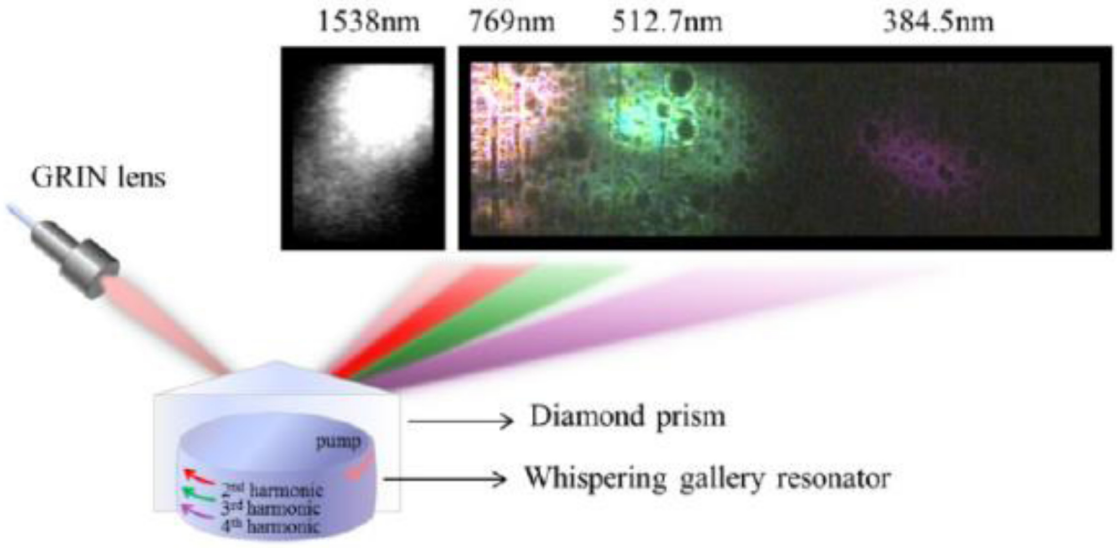

Figure 7.5: Visual verification of fourth harmonic generation: A pump beam is recorded with an infrared CCD camera, and the harmonics are observed on a color CCD coated with ultraviolet fluorescent ink. The second, third, and fourth, harmonics are present simultaneously.

7.6 Efficient Broad-Band Pumping of High-Quality, Micro-Lasers

Many on-chip optical applications, including spectroscopy, sensing, nonlinear optics, and optical communications require high-finesse, high-quality factor (high-Q) micro-lasers. Such lasers must be exceptionally transparent at their emission wavelength. But if high- Q micro lasers exhibit correspondingly weak absorption at the pump wavelengths, they are challenging to excite. Here, we demonstrate micro-ring lasers that exhibit Q ¿ $5.2x10^6$ and a finesse of $> 1.8x10^4$ with a direct-illumination,

non-resonant pump (9). The micro-rings are coated with a combination of three organic dyes as in Figure 7.6. This cascaded combination of near and ultimately far field energy transfer reduces material losses by a factor of more than 10^4 , transforming incoherent light to coherent light with high quantum-efficiency. The operating principle established here is general and can enable fully integrated on-chip, high finesse micro lasers without the complications of coupled pump and emitter resonators. This work was reported in Advanced Materials (9).

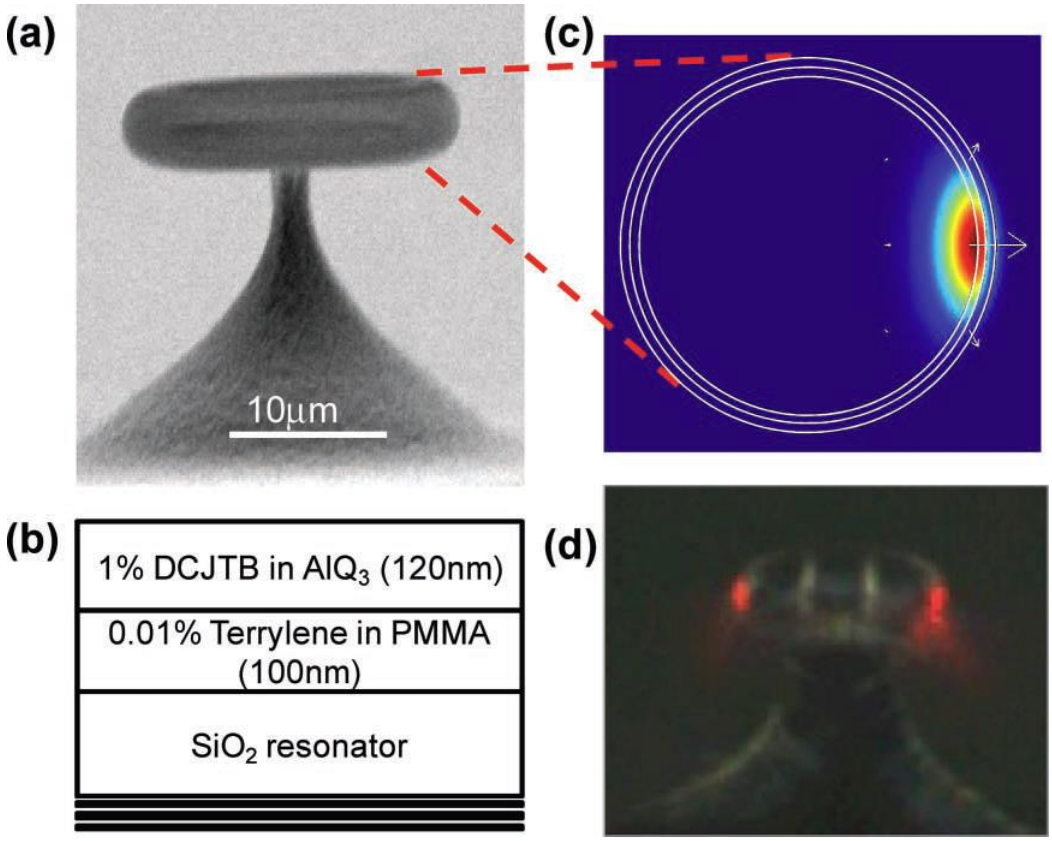

Figure 7.6: (a) A typical micro-ring resonator. (b) The structure of the gain materials deposited on the resonator. (c) Numerical simulation of the lasing mode with polarization indicated by the arrows, and (d), a typical example of lasing.

7.7 Intensity enhancement with a nanoparticle coupled to a microtoroid

We present an optical mode solver for a whispering gallery resonator coupled to an adjacent arbitrary shaped (as in Figure 7.7 nano-particle that breaks the axial symmetry of the resonator (10). Such a hybrid resonator-nanoparticle is similar to what was recently used for bio-detection and for field enhancement. We demonstrate our solver by parametrically studying a toroid-nanoplasmonic device and get the optimal nano-plasmonic size for maximal enhancement. We investigate cases near a plasmonic resonance as well as far from a plasmonic resonance. Unlike common plasmons that typically benefit from working near their resonance, here working far from plasmonic resonance provides comparable performance. This is because the plasmonic resonance enhancement is accompanied by cavity quality degradation through plasmonic absorption. This work was reported in Optics Express (10).

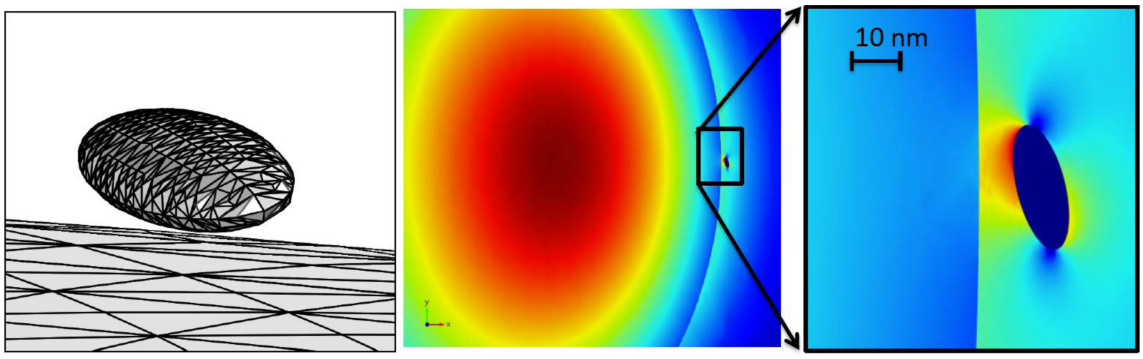

Figure 7.7: Solution for a non-symmetrical nanoparticle configuration. A gold ellipsoid with semiaxis lengths of 10, 20 and 200 nm was located 24 nm away from a silica toroid that is resonating at 1.55 μm vacuum wavelength. The ellipsoid is rotated at an arbitrary angle along an arbitrary direction vector. Color represents normalized electric field.

REFERENCES

[1] A. A. Savchenkov, A. B. Matsko, V. S. Ilchenko, D. Strekalov, and L. Maleki, "Direct observation of stopped light in a whispering-gallery-mode microresonator," *Physical Review A*, vol. 76, p. 23816, Aug. 2007.

[2] T. Carmon, H. G. L. Schwefel, L. Yang, M. Oxborrow, A. D. Stone, and K. J. Vahala, "Static Envelope Patterns in Composite Resonances Generated by Level Crossing in Optical Toroidal Microcavities," *Physical Review Letters*, vol. 100, p. 103905, Mar. 2008.

[3] G. Bahl, J. Zehnpfennig, M. Tomes, and T. Carmon, "Stimulated optomechanical excitation of surface acoustic waves in a microdevice," *Nature Communications*, vol. 2, p. 403, July 2011.

[4] G. Bahl, M. Tomes, F. Marquardt, and T. Carmon, "Observation of spontaneous Brillouin cooling," *Nature Physics*, vol. 8, pp. 203–207, Jan. 2012.

[5] J. Zehnpfennig, G. Bahl, M. Tomes, and T. Carmon, "Surface optomechanics : calculating optically excited acoustical whispering gallery modes in microspheres," *Optics Express*, vol. 19, no. 15, pp. 14240–14248, 2011.

[6] X. Zhang, M. Tomes, and T. Carmon, "Precession optomechanics," *Optics Express*, vol. 19, no. 10, pp. 9066–9073, 2011.

[7] J. Moore, M. Tomes, T. Carmon, and M. Jarrahi, "Continuous-wave ultraviolet emission through fourth-harmonic generation in a whispering- gallery resonator," *Optics Express*, vol. 19, no. 24, pp. 24139–24146, 2011.

[8] J. Moore, M. Tomes, T. Carmon, and M. Jarrahi, "Continuous-wave cascaded-harmonic generation and multi-photon Raman lasing in lithium niobate whispering-gallery resonators," *Applied Physics Letters*, vol. 99, no. 22, p. 221111, 2011.

[9] C. Rotschild, M. Tomes, H. Mendoza, T. Carmon, and M. Baldo, "Cascaded energy transfer for efficient broad-band pumping of high-quality, micro-lasers," *Accepted for publication at Advanced Materials*, 2011.

[10] A. Kaplan, M. Tomes, T. Carmon, M. Kozlov, O. Cohen, G. Bartal, and H. G. L. Schwefel, "Finite element simulation of a perturbed axial-symmetric whispering-gallery mode and its use for intensity enhancement with a nanoparticle coupled to a microtoroid," *Optics Express*, vol. 21, p. 14169, June 2013.

CHAPTER VIII

Summary and Future Work

To conclude, we reported on the first backward stimulated Brillouin scattering in micro scaled devices. Further, it allowed operating at high vibration rates (11 GHz) (1) by transforming the mechanical frequency to depend on optical wavelength, rather than device size as before. We also reported on the first forward stimulated Brillouin scattering in micro scaled devices which allowed 50-1500 MHz mechanical oscillations with mechanical quality factors over 10,000 (2). As explained in (3) the long phonon lifetime associated with the above quality factor allowed us to access a regime where we demonstrated for the first time in any system in nature, reversing the energy transfer direction in a light-sound Brillouin scattering interaction to support cooling (4). This is indicated by a decrease in scattering as the pump increases in power in contrast with previous works where scattering increases with pump power.

This work will be beneficial to future work in the new field of Brillouin optomechanics. There are three directions I would like to highlight.

8.1 Commercial oscillators

It is important for time measurement and travel without GPS to have a stable and low phase noise oscillator to act as a portable time standard. Among the publications in which our work was cited is the extension of Brillouin optomechanics to on chip

devices. Researchers at Caltech have designed an centimeter scale, on-chip silica micro disk resonator with a free spectral range designed to phasematch 11 GHz oscillations (5). Benefits include many orders of cascaded generation and lowered phase noise (6). This work has been commercialized at a startup in Pasedena called HQPhotonics.

8.2 Micro-fluidics

Optomechanical fluidics has been proposed for ultrasonic image sensors and for fundamental studies of optomechanics with super fluids at the quantum domain. In this manner, we have extended this work to the demonstration of Brillouin optomechanics in micro fluidic resonators (8). Recently, micro-fluidic resonators have demonstrated both breathe mode optomechanics (7) and Brillouin optomechanics (8). The acoustical whispering gallery modes in a micro-fluidic shell have been analyzed to determine their frequency and mode profiles (9). Micro-fluidic optomechanics can allow sensing in liquids that are not transparent to the optical wavelength, as resonators can be designed in which only the mechanical mode reaches the inside surface (9).

8.3 Raman cooling

As the cooling quantum efficiency scales as Ω_m/ω, where Ω_m is the phonon angular frequency and ω_m is the photon angular frequency, it is implied that the Brillouin cooling quantum efficiency is low. Since the optical phonon involved in Raman scattering is at terahertz frequencies, the cooling quantum efficiency should be as much as 1000 times higher. This could allow cooling the thermal bath instead of a single mechanical mode. We suggest that the selective filtering of light used in our demonstration of Brillouin cooling can potentially enable Raman cooling. Despite many challenges, including the short lifetime of the Raman optical phonon, Raman cooling

does not contradict the laws of physics and should be investigated.

REFERENCES

[1] M. Tomes and T. Carmon, "Photonic Micro-Electromechanical Systems Vibrating at X-band (11-GHz) Rates," *Physical Review Letters*, vol. 102, p. 113601, Mar. 2009.

[2] G. Bahl, J. Zehnpfennig, M. Tomes, and T. Carmon, "Stimulated optomechanical excitation of surface acoustic waves in a microdevice," *Nature Communications*, vol. 2, p. 403, July 2011.

[3] T. J. Kippenberg and K. J. Vahala, "Cavity opto-mechanics: Back-Action at the Mesoscale," *Science*, vol. 321, pp. 1172–1176, Dec. 2008.

[4] G. Bahl, M. Tomes, F. Marquardt, and T. Carmon, "Observation of Spontaneous Brillouin Cooling," *ArXiv e-prints*, Sept. 2011.

[5] H. Lee, T. Chen, J. Li, K. Y. Yang, S. Jeon, O. Painter, and K. J. Vahala, "Chemically etched ultrahigh-Q wedge-resonator on a silicon chip," *Nature Photonics*, vol. 6, pp. 369–373, May 2012.

[6] J. Li, H. Lee, T. Chen, and K. Vahala, "Characterization of a high coherence, Brillouin microcavity laser on silicon," *Optics Express*, vol. 20, no. 18, pp. 369–373, 2012.

[7] K. H. Kim, G. Bahl, W. Lee, J. Liu, M. Tomes, X. Fan, and T. Carmon, "Cavity optomechanics on a microfluidic resonator with water and viscous liquids," *ArXiv e-prints*, pp. 1–12, 2013.

[8] G. Bahl, K. H. Kim, W. Lee, J. Liu, X. Fan, and T. Carmon, "Brillouin cavity optomechanics with microfluidic devices.," *Nature communications*, vol. 4, p. 1994, June 2013.

[9] G. Bahl, X. Fan, and T. Carmon, "Acoustic whispering-gallery modes in optomechanical shells," *New Journal of Physics*, vol. 14, p. 115026, Nov. 2012.

APPENDIX

APPENDIX A

Going from classical equations of motion to phonon occupation numbers

This appendix details the math needed to transform the classical equations of motion given in (5.9) to the phonon occupancy numbers given in (5.14). Here are the starting classical equations are repeated below:

$$\dot{\alpha_1} = \left[i\Delta - \frac{\kappa_1}{2}\right]\alpha_1 + \frac{\kappa_1}{2}\alpha_1^{max} - ig\alpha_2\beta^*, \tag{A.1}$$

$$\dot{\alpha_2} = \left[i\left(\Delta - \delta\omega\right) - \frac{\kappa_2}{2}\right]\alpha_2 - ig\alpha_1\beta, \tag{A.2}$$

$$\dot{\beta} = \left[-i\Omega - \frac{\Gamma}{2}\right]\beta + \sqrt{n_{th}\Gamma}\xi(t) - ig\alpha_2\alpha_1^*. \tag{A.3}$$

We assume that we are pumping on resonance and can set $\Delta = 0$.

$$\dot{\alpha_1} = -\frac{\kappa_1}{2}\alpha_1 + \frac{\kappa_1}{2}\alpha_1^{max} - ig\alpha_2\beta^*, \tag{A.4}$$

$$\dot{\alpha_2} = \left[-i\delta\omega - \frac{\kappa_2}{2}\right]\alpha_2 - ig\alpha_1\beta, \tag{A.5}$$

$$\dot{\beta} = \left[-i\Omega - \frac{\Gamma}{2}\right]\beta + \sqrt{n_{th}\Gamma}\xi(t) - ig\alpha_2\alpha_1^*. \tag{A.6}$$

Then we linearize the solution around $(\alpha_1, \alpha_2, \beta) = (\alpha_1^{max}, 0, 0)$. Additionally, we assume that the mechanical mode frequency Ω is exactly equal to the optical mode spacing $\delta\omega$. Thus we can replace $\delta\omega$ with Ω.

$$\dot{\alpha_1} = 0, \tag{A.7}$$

$$\dot{\alpha_2} = \left[-i\Omega - \frac{\kappa_2}{2}\right]\alpha_2 - ig\alpha_1^{max}\beta, \tag{A.8}$$

$$\dot{\beta} = \left[-i\Omega - \frac{\Gamma}{2}\right]\beta + \sqrt{n_{th}\Gamma}\xi(t) - ig\alpha_2\alpha_1^{max*}. \tag{A.9}$$

Next, I will need to list a few Fourier transform pairs that will be required for the derivation.

$$u(t)e^{-\alpha t} \Leftrightarrow \frac{1}{\alpha + i\omega}, \tag{A.10}$$

$$\dot{f}(t) \Leftrightarrow i\omega F(\omega), \tag{A.11}$$

$$f(t)e^{i\Omega t} \Leftrightarrow F(\omega - \Omega). \tag{A.12}$$

A.1 Solving for Beta

The next section begins by solving for β. After that, we will determine $|\beta(t)|^2$. The same derivations for α and $|\alpha(t)|^2$ will follow. The first tep in solving for β is to take the Fourier transform of equations (A.8) and (A.9).

$$i\omega\alpha_2(\omega) = [-i\Omega - \frac{\kappa_2}{2}]\alpha_2 - ig\alpha_1^{max}\beta(\omega), \tag{A.13}$$

$$i\omega\beta(\omega) = [-i\Omega - \frac{\Gamma_2}{2}]\beta - ig\alpha_1^{max*}\alpha_2(\omega) + \sqrt{n_{th}\Gamma}\xi(\omega). \tag{A.14}$$

After simplifying:

$$\alpha_2(\omega) = \frac{1}{\left(i\left(\omega+\Omega\right)+\frac{\kappa_2}{2}\right)}\left(-ig\alpha_1^{max}\beta(\omega)\right), \tag{A.15}$$

$$\beta(\omega) = \frac{1}{\left(i\left(\omega+\Omega\right)+\frac{\Gamma_2}{2}\right)}\left(-ig\alpha_1^{max*}\alpha_2(\omega)+\sqrt{n_{th}\Gamma}\xi(\omega)\right). \tag{A.16}$$

Then we substitute (A.15) into (A.16) to get an expression that depends only on $\beta(\omega)$.

$$\beta(\omega) = \frac{1}{\left(i\left(\omega+\Omega\right)+\frac{\Gamma_2}{2}\right)}\left(-ig\alpha_1^{max*}\left(\frac{1}{\left(i\left(\omega+\Omega\right)+\frac{\kappa_2}{2}\right)}\left(-ig\alpha_1^{max}\beta(\omega)\right)\right)+\sqrt{n_{th}\Gamma}\xi(\omega)\right). \tag{A.17}$$

Pulling all the terms that depend on $\beta(\omega)$ to one side results in:

$$\left[\left(i\left(\omega+\Omega\right)+\frac{\Gamma}{2}\right)\left(i\left(\omega+\Omega\right)+\frac{\kappa}{2}\right)+g^2|\alpha_1^{max}|^2\right]\beta(\omega) = \left(i\left(\omega+\Omega\right)+\frac{\kappa}{2}\right)\sqrt{n_{th}\Gamma}\xi(\omega), \tag{A.18}$$

and the final expression for $\beta(\omega)$ is:

$$\beta(\omega) = \frac{1}{\left[\left(i\left(\omega+\Omega\right)+\frac{\Gamma}{2}\right)\left(i\left(\omega+\Omega\right)+\frac{\kappa}{2}\right)+g^2|\alpha_1^{max}|^2\right]}\left(i\left(\omega+\Omega\right)+\frac{\kappa}{2}\right)\sqrt{n_{th}\Gamma}\xi(\omega). \tag{A.19}$$

Next, to make the math simpler, we substitute $i\left(\omega+\Omega\right)=\sigma$.

$$\beta(\omega) = \frac{1}{\left[\left(\sigma+\frac{\Gamma}{2}\right)\left(\sigma+\frac{\kappa}{2}\right)+g^2|\alpha_1^{max}|^2\right]}\left(\sigma+\frac{\kappa}{2}\right)\sqrt{n_{th}\Gamma}\xi(\omega). \tag{A.20}$$

We then expand the denominator to prepare to take the partial fraction expansion.

$$\beta(\omega) = \frac{\sigma + \frac{\kappa}{2}}{\sigma^2 + \left(\frac{\Gamma}{2} + \frac{\kappa}{2}\right)\sigma + \frac{\Gamma\kappa}{4} + g^2|\alpha_1^{max}|^2}\sqrt{n_{th}\Gamma}\xi(\omega). \tag{A.21}$$

Now we find the roots of the denominator for the purpose of partial fraction expansion.

$$\beta(\omega) = \frac{\sigma + \frac{\kappa}{2}}{(\sigma - s_1)(\sigma - s_2)}\sqrt{n_{th}\Gamma}\xi(\omega), \tag{A.22}$$

$$s_{1,2} = \frac{-b \pm \sqrt{b^2 - 4ac}}{2}, \tag{A.23}$$

$$s_{1,2} = \frac{-\left(\frac{\Gamma}{2} + \frac{\kappa}{2}\right) \pm \sqrt{\left(\frac{\Gamma}{2} + \frac{\kappa}{2}\right)^2 - 4\left(\frac{\Gamma\kappa}{4} + g^2|\alpha_1^{max}|^2\right)}}{2}. \tag{A.24}$$

Now we perform partial fraction expansion on the above expression.

$$\frac{\sigma + \frac{\kappa}{2}}{(\sigma - s_1)(\sigma - s_2)} = \frac{c_1}{(\sigma - s_1)} + \frac{c_2}{(\sigma - s_2)}, \tag{A.25}$$

$$c_1 = \frac{s_1 + \frac{\kappa}{2}}{s_1 - s_2}, \tag{A.26}$$

$$c_2 = \frac{s_2 + \frac{\kappa}{2}}{s_2 - s_1}, \tag{A.27}$$

$$\beta(\omega) = \left(\frac{c_1}{(\sigma - s_1)} + \frac{c_2}{(\sigma - s_2)}\right)\sqrt{n_{th}\Gamma}\xi(\omega). \tag{A.28}$$

We take this expression for $\beta(\omega)$ and take the inverse Fourier transform of it. It will be the convolution of the inverse Fourier transform of the two parts.

$$\beta(t) = \left(c_1 e^{s_1 t} e^{-i\Omega t} + c_2 e^{s_2 t} e^{-i\Omega t}\right) \otimes \sqrt{n_{th}\Gamma}\xi(t), \tag{A.29}$$

$$\beta(t) = \int_{-inf}^{t} \left(c_1 e^{s_1(t-\tau)} e^{-i\Omega(t-\tau)} + c_2 e^{s_2(t-\tau)} e^{-i\Omega(t-\tau)}\right) \sqrt{n_{th}\Gamma}\xi(\tau)d\tau. \tag{A.30}$$

This has given us an expression for $\beta(t)$, but we are really looking for an expression for $\langle|\beta(t)|^2\rangle$.

$$|\beta(t)|^2 = n_{th}\Gamma \int_{-inf}^{t}\int_{-inf}^{t} \left(c_1 e^{s_1(t-\tau_1)} e^{-i\Omega(t-\tau_1)} + c_2 e^{s_2(t-\tau_1)} e^{-i\Omega(t-\tau_1)}\right) \tag{A.31}$$
$$\left(c_1^* e^{s_1^*(t-\tau_2)} e^{i\Omega(t-\tau_2)} + c_2^* e^{s_2^*(t-\tau_2)} e^{i\Omega(t-\tau_2)}\right) \xi(\tau_1)\xi^*(\tau_2)d\tau_1 d\tau_2.$$

We can simplify knowing that $\xi(\tau_1)\xi^*(\tau_2) = \delta(\tau_2 - \tau_1)$ which will allow us to easily take the first integral.

$$\langle|\beta(t)|^2\rangle = n_{th}\Gamma \int_{-inf}^{t}\int_{-inf}^{t} \left(c_1 e^{s_1(t-\tau_1)} e^{-i\Omega(t-\tau_1)} + c_2 e^{s_2(t-\tau_1)} e^{-i\Omega(t-\tau_1)}\right) \tag{A.32}$$
$$\left(c_1^* e^{s_1^*(t-\tau_2)} e^{i\Omega(t-\tau_2)} + c_2^* e^{s_2^*(t-\tau_2)} e^{i\Omega(t-\tau_2)}\right) \delta(\tau_2 - \tau_1)d\tau_1 d\tau_2.$$

Here we take the first integral and then we will simplify by pulling out the exponentials which depend on Ω.

$$\langle|\beta(t)|^2\rangle = n_{th}\Gamma \int_{-inf}^{t} \left(c_1 e^{s_1(t-\tau_2)} e^{-i\Omega(t-\tau_2)} + c_2 e^{s_2(t-\tau_2)} e^{-i\Omega(t-\tau_2)}\right) \left(c_1^* e^{s_1^*(t-\tau_2)} e^{i\Omega(t-\tau_2)} + c_2^* e^{s_2^*(t-\tau_2)} e^{i\Omega(t-\tau_2)}\right) d\tau_2, \tag{A.33}$$

$$\langle|\beta(t)|^2\rangle = n_{th}\Gamma \int_{-inf}^{t} \left(c_1 e^{s_1(t-\tau_2)} + c_2 e^{s_2(t-\tau_2)}\right) \left(c_1^* e^{s_1^*(t-\tau_2)} + c_2^* e^{s_2^*(t-\tau_2)}\right) d\tau_2. \tag{A.34}$$

Then we foil the two multiplied terms:

$$\langle|\beta(t)|^2\rangle = n_{th}\Gamma \int_{-inf}^{t} (|c_1|^2 e^{(s_1+s_1^*)(t-\tau_2)} + (c_1 c_2^*) e^{(s_1+s_2^*)(t-\tau_2)} + (c_1^* c_2) e^{(s_1^*+s_2)(t-\tau_2)} + |c_2|^2 e^{(s_2+s_2^*)(t-\tau_2)}) d\tau_2. \tag{A.35}$$

The expression simplifies as $s_2 + s_2^* = 2Re[s_2]$.

$$\langle|\beta(t)|^2\rangle = n_{th}\Gamma \int_{-inf}^{t} (|c_1|^2 e^{2Re[s_1](t-\tau_2)} + (c_1 c_2^*) e^{(s_1+s_2^*)(t-\tau_2)} + (c_1^* c_2) e^{(s_1^*+s_2)(t-\tau_2)} + |c_2|^2 e^{2Re[s_2](t-\tau_2)}) d\tau_2. \tag{A.36}$$

Finally, we take the last integral and will evaluate from $-\inf$ to t.

$$\langle|\beta(t)|^2\rangle = n_{th}\Gamma \tag{A.37}$$

$$\left|-\frac{|c_1|^2}{2Re[s_1]}e^{2Re[s_1](t-\tau_2)} - \frac{(c_1c_2^*)}{s_1+s_2^*}e^{(s_1+s_2^*)(t-\tau_2)} - \frac{(c_1^*c_2)}{s_1^*+s_2}e^{(s_1^*+s_2)(t-\tau_2)} - \frac{|c_2|^2}{2Re[s_2]}e^{2Re[s_2](t-\tau_2)}\right|_{-inf}^{t}.$$

Here, both $Re[s_1]$ and $Re[s_2]$ must be negative so that the exponentials go to zero when τ_2 goes to negative infinity. This is verified to be true in mathematica. Thus we have our final expression for $\langle|\beta(t)|^2\rangle$.

$$\langle|\beta(t)|^2\rangle = -n_{th}\Gamma\left(\frac{|c_1|^2}{2Re[s_1]} + \frac{(c_1c_2^*)}{s_1+s_2^*} + \frac{(c_1^*c_2)}{s_1^*+s_2} + \frac{|c_2|^2}{2Re[s_2]}\right). \tag{A.38}$$

This concludes the derivation of $\langle|\beta(t)|^2\rangle$.

A.2 Solving for Alpha

Next we derive $\langle|\alpha_2(t)|^2\rangle$. Going back to equations (A.15) and (A.16), we substitute to get an expression that relies only on $\alpha_2(\omega)$.

$$\alpha_2(\omega) = \frac{1}{\left(\sigma+\frac{\kappa_2}{2}\right)}\left(-ig\alpha_1^{max}\left[\frac{1}{\left(\sigma+\frac{\Gamma_2}{2}\right)}\left(-ig\alpha_1^{max*}\alpha_2(\omega) + \sqrt{n_{th}\Gamma}\xi(\omega)\right)\right]\right). \tag{A.39}$$

Pulling all the terms that depend on $\beta(\omega)$ to one side results in:

$$\alpha_2(\omega) = \frac{1}{\left(\left(\sigma+\frac{\kappa_2}{2}\right)\left(\sigma+\frac{\Gamma_2}{2}\right) + g^2|\alpha_1^{max}|^2\right)}\left(-ig\alpha_1^{max}\sqrt{n_{th}\Gamma}\xi(\omega)\right). \tag{A.40}$$

We have the same demoninator as before.

$$\alpha_2(\omega) = \frac{1}{(\sigma - s_1)(\sigma - s_2)} \left(-ig\alpha_1^{max} \sqrt{n_{th}\Gamma}\xi(\omega) \right). \tag{A.41}$$

We use partial fraction expansion again.

$$\frac{1}{(\sigma - s_1)(\sigma - s_2)} = \frac{c_3}{(\sigma - s_1)} + \frac{c_4}{(\sigma - s_2)}, \tag{A.42}$$

$$c_3 = \frac{1}{s_1 - s_2}, \tag{A.43}$$

$$c_4 = \frac{1}{s_2 - s_1}, \tag{A.44}$$

$$\alpha_2(\omega) = \left(\frac{c_3}{(\sigma - s_1)} + \frac{c_4}{(\sigma - s_2)} \right) \left(-ig\alpha_1^{max} \sqrt{n_{th}\Gamma}\xi(\omega) \right). \tag{A.45}$$

Once again we see the inverse Fourier transform will be a convolution of the two terms.

$$\alpha_2(t) = \left(c_3 e^{s_1 t} e^{-i\Omega t} + c_4 e^{s_2 t} e^{-i\Omega t} \right) \otimes \left(-ig\alpha_1^{max} \sqrt{n_{th}\Gamma}\xi(t) \right), \tag{A.46}$$

$$\alpha_2(t) = \int_{-inf}^{t} \left(c_3 e^{s_1(t-\tau)} e^{-i\Omega(t-\tau)} + c_4 e^{s_2(t-\tau)} e^{-i\Omega(t-\tau)} \right) \left(-ig\alpha_1^{max} \sqrt{n_{th}\Gamma}\xi(\tau) \right) d\tau. \tag{A.47}$$

Again we have an expression for $\alpha(t)$, but we are really looking for an expression for $\langle |\alpha(t)|^2 \rangle$.

$$|\alpha_2(t)|^2 = g^2|\alpha_1^{max}|^2 n_{th}\Gamma \int_{-inf}^{t}\int_{-inf}^{t} \left(c_3 e^{s_1(t-\tau_1)}e^{-i\Omega(t-\tau_1)} + c_4 e^{s_2(t-\tau_1)}e^{-i\Omega(t-\tau_1)}\right) \left(c_3^* e^{s_1^*(t-\tau_2)}e^{i\Omega(t-\tau_2)} + c_4^* e^{s_2^*(t-\tau_2)}e^{i\Omega(t-\tau_2)}\right) \xi(\tau_1)\xi(\tau_2)^* d\tau_1 d\tau_2. \quad \text{(A.48)}$$

We follow the same steps as before starting with the simplification: $\xi(\tau_1)\xi^*(\tau_2) = \delta(\tau_2 - \tau_1)$.

$$\langle|\alpha_2(t)|^2\rangle = g^2|\alpha_1^{max}|^2 n_{th}\Gamma \int_{-inf}^{t}\int_{-inf}^{t} \left(c_3 e^{s_1(t-\tau_1)}e^{-i\Omega(t-\tau_1)} + c_4 e^{s_2(t-\tau_1)}e^{-i\Omega(t-\tau_1)}\right) \left(c_3^* e^{s_1^*(t-\tau_2)}e^{i\Omega(t-\tau_2)} + c_4^* e^{s_2^*(t-\tau_2)}e^{i\Omega(t-\tau_2)}\right) \delta(\tau_2 - \tau_1) d\tau_1 d\tau_2. \quad \text{(A.49)}$$

We take the first integral:

$$\langle|\alpha_2(t)|^2\rangle = g^2|\alpha_1^{max}|^2 n_{th}\Gamma \int_{-inf}^{t} \left(c_3 e^{s_1(t-\tau_2)}e^{-i\Omega(t-\tau_2)} + c_4 e^{s_2(t-\tau_2)}e^{-i\Omega(t-\tau_2)}\right) \left(c_3^* e^{s_1^*(t-\tau_2)}e^{i\Omega(t-\tau_2)} + c_4^* e^{s_2^*(t-\tau_2)}e^{i\Omega(t-\tau_2)}\right) d\tau_2. \quad \text{(A.50)}$$

Then we will simplify by pulling out the exponentials which depend on Ω.

$$\langle|\alpha_2(t)|^2\rangle = g^2|\alpha_1^{max}|^2 n_{th}\Gamma \int_{-inf}^{t} \left(c_3 e^{s_1(t-\tau_2)} + c_4 e^{s_2(t-\tau_2)}\right) \left(c_3^* e^{s_1^*(t-\tau_2)} + c_4^* e^{s_2^*(t-\tau_2)}\right) d\tau_2. \quad \text{(A.51)}$$

Then we foil the two multiplied terms:

$$\langle|\alpha_2(t)|^2\rangle = g^2|\alpha_1^{max}|^2 n_{th}\Gamma \int_{-inf}^{t} \tag{A.52}$$
$$\left(|c_3|^2 e^{(s_1+s_1^*)(t-\tau_2)} + (c_3 c_4^*)e^{(s_1+s_2^*)(t-\tau_2)} + (c_3^* c_4)e^{(s_1^*+s_2)(t-\tau_2)} + |c_4|^2 e^{(s_2+s_2^*)(t-\tau_2)}\right) d\tau_2,$$

$$\langle|\alpha_2(t)|^2\rangle = g^2|\alpha_1^{max}|^2 n_{th}\Gamma \int_{-inf}^{t} \tag{A.53}$$
$$\left(|c_3|^2 e^{2Re[s_1](t-\tau_2)} + (c_3 c_4^*)e^{(s_1+s_2^*)(t-\tau_2)} + (c_3^* c_4)e^{(s_1^*+s_2)(t-\tau_2)} + |c_4|^2 e^{2Re[s_2](t-\tau_2)}\right) d\tau_2.$$

Finally, we take the last integral and will evaluate from $-\inf$ to t.

$$\langle|\alpha_2(t)|^2\rangle = g^2|\alpha_1^{max}|^2 n_{th}\Gamma \tag{A.54}$$
$$\left|\frac{-|c_3|^2}{2Re[s_1]}e^{2Re[s_1](t-\tau_2)} - \frac{(c_3 c_4^*)}{(s_1+s_2^*)}e^{(s_1+s_2^*)(t-\tau_2)} - \frac{(c_3^* c_4)}{(s_1^*+s_2)}e^{(s_1^*+s_2)(t-\tau_2)} - \frac{|c_4|^2}{2Re[s_2]}e^{2Re[s_2])(t-\tau_2)}\right|_{-inf}^{t}.$$

Here, both $Re[s_1]$ and $Re[s_2]$ must be negative so that the exponentials go to zero when τ_2 goes to negative infinity. This is verified to be true in mathematica. Thus we have our final expression for $\langle|\alpha(t)|^2\rangle$.

$$\langle|\alpha_2(t)|^2\rangle = -g^2|\alpha_1^{max}|^2 n_{th}\Gamma\left(\frac{|c_3|^2}{2Re[s_1]} + \frac{(c_3 c_4^*)}{(s_1+s_2^*)} + \frac{(c_3^* c_4)}{(s_1^*+s_2)} + \frac{|c_4|^2}{2Re[s_2]}\right). \tag{A.55}$$

This concludes the derivation of $\langle|\alpha(t)|^2\rangle$ and this appendix.